



13 **Abstract**

14 Land evapotranspiration (ET) plays a crucial role in Earth's water-carbon cycle, and
15 accurately estimating global land ET is vital for advancing our understanding of land-
16 atmosphere interactions. Despite the development of numerous ET products in recent
17 decades, widely used products still possess inherent uncertainties arising from using
18 different forcing inputs and imperfect model parameterizations. Furthermore, the lack
19 of sufficient global in-situ observations makes direct evaluation of ET products
20 impractical, impeding their utilization and assimilation. Therefore, establishing a
21 reliable global benchmark dataset and exploring evaluation methodologies for ET
22 products is paramount. This study aims to address these challenges by (1) proposing a
23 collocation-based method that considers non-zero error cross-correlation for merging
24 multi-source data and (2) employing this merging method to generate a long-term
25 daily global ET product at resolutions of 0.1° (2000-2020) and 0.25° (1980-2022),
26 incorporating inputs from ERA5L, FluxCom, PMLv2, GLDAS, and GLEAM. The
27 resulting product is the Collocation-Analyzed Multi-source Ensembled Land
28 Evapotranspiration Data (CAMELE). CAMELE exhibits excellent performance
29 across various vegetation coverage types, as validated against in-situ observations.
30 The evaluation process yielded Pearson correlation coefficients (R) of 0.63 and 0.65,
31 root-mean-square-errors (RMSE) of 0.81 and 0.73 mm/d, unbiased root-mean-square-
32 errors (ubRMSE) of 1.20 and 1.04 mm/d, mean absolute errors (MAE) of 0.81 and
33 0.73 mm/d, and Kling-Gupta efficiency (KGE) of 0.60 and 0.65 on average over
34 resolutions of 0.1° and 0.25° , respectively.

35 **1. Introduction**

36 Land evapotranspiration (ET) plays a critical role in the global water and energy
37 cycles, encompassing various processes such as soil evaporation, vegetation
38 transpiration, canopy interception, and surface water evaporation (Zhang et al., 2019;



39 Zhao et al., 2022; Lian et al., 2018). Accurately estimating global land
40 evapotranspiration is vital for understanding the hydrological cycle and land-
41 atmosphere interactions, as it serves as an intermediary variable connecting soil
42 moisture and air temperature (Miralles et al., 2019; Gentine et al., 2019). Therefore,
43 providing a reliable ET dataset as a benchmark for further research is crucial.

44 In recent decades, numerous studies have focused on estimating global land
45 evapotranspiration, resulting in many datasets. However, discrepancies often arise
46 among these simulations due to algorithm and principle variations (Restrepo-Coupe et
47 al., 2021; Han and Tian, 2020). Additionally, evaluating ET products is challenging
48 due to the limited availability of global-scale observations, which hampers their direct
49 use (Pan et al., 2020; Baker et al., 2021).

50 The fusion of multi-source data is a suitable option to address these uncertainties.
51 Recent studies have explored several approaches to integrate multiple ET products,
52 including Simple Average (SA) (Ershadi et al., 2014), Bayesian Model Average
53 (BMA) (Hao et al., 2019; Ma et al., 2020; Zhu et al., 2016), Reliability Ensemble
54 Average (REA) (Lu et al., 2021), Empirical Orthogonal Functions (EOF) (Feng et al.,
55 2016) and machine-learning-based methods (Chen et al., 2020; Yin et al., 2021).
56 However, the primary challenge lies in calculating reliable input weights based on a
57 selected "truth" (Koster et al., 2021), which can involve averaging or incorporating
58 other relevant geographical information as a benchmark. Moreover, previous research
59 has predominantly focused on regional-scale ET estimation, necessitating a more
60 straightforward and reliable global simulation method.

61 Recently, collocation methods have emerged as promising techniques for estimating
62 random error variances and data-truth correlations in collocated inputs (Stoffelen,
63 1998; Li et al., 2022, 2023b; Park et al., 2023). These methods consider the errors
64 associated with collocated datasets as an accurate representation of uncertainty
65 without assuming the absence of errors in any datasets. It is important to note that
66 while collocation methods, such as TC and EIVD, can estimate the variance (or



67 covariance) of random errors, they cannot evaluate the bias of the products. One
68 primary advantage of collocation analysis is that it does not require a high-quality
69 reference dataset (Su et al., 2014; Wu et al., 2021). However, a crucial prerequisite for
70 applying collocation methods is the availability of many spatially and temporally
71 corresponding datasets. For instance, the classic triple collocation (TC) method
72 requires a trio of independent datasets. Su et al. (2014) used the instrumental
73 regression method and considered lag-1 time series as the third input, proposing the
74 single instrumental variable algorithm (IVS). Dong et al. (2019) introduced the lag-1
75 time series from both inputs, proposing the double instrumental variable algorithm
76 (IVD) for a more robust solution. Gruber et al. (2016a) extended the original
77 algorithm to incorporate more datasets, partially addressing the independence
78 assumption to calculate a portion of error cross-correlation (ECC). Dong et al. (2020a)
79 further proposed the extended double instrumental (EIVD) method, enabling ECC
80 estimation using three datasets. Collocation methods have found widespread
81 application in the evaluation of geophysical variable estimates, including soil
82 moisture (Deng et al., 2023; Ming et al., 2022), precipitation (Dong et al., 2022; Li et
83 al., 2018), ocean wind speed (Vogelzang et al., 2022; Ribal and Young, 2020), leaf
84 area index (Jiang et al., 2017), total water storage (Yin and Park, 2021) sea ice
85 thickness and surface salinity (Hoareau et al., 2018), and near-surface air temperature
86 (Sun et al., 2021).

87 Recently, many studies have utilized collocation approaches to evaluate
88 evapotranspiration products, with the TC method to assess uncertainties. For example,
89 Barraza Bernadas et al. (2018) considered the uncertainties of ET from the Breathing
90 Earth System Simulator, BESS (Jiang et al., 2020; Jiang and Ryu, 2016), Moderate
91 Resolution Imaging Spectroradiometer, MOD16 (Mu et al., 2011), and a hybrid
92 model; Khan et al. (2018) utilized extended triple collocation (ETC) (McColl et al.,
93 2014) to investigate the reliability of ET from MOD16, The Global Land Data
94 Assimilation System (GLDAS) (Rodell et al., 2004) and the Global Land Evaporation



95 Amsterdam Model (GLEAM) (Martens et al., 2017) over East Asia; Li et al. (2022)
96 employed five collocation methods (e.g., IVS, IVD, TC, EIVD, and EC) to analyze
97 the uncertainties of ET from ERA5-Land (ERA5L) (Muñoz-Sabater et al., 2021),
98 GLEAM, GLDAS, FluxCom (Jung et al., 2019), and the Penman-Monteith-Leuning
99 Evapotranspiration V2 (PMLv2) (Zhang et al., 2019).

100 Moreover, error information derived from collocation analysis is valuable for merging
101 multi-source ET data. Park et al. (2023) combined three reanalysis-based evaporation
102 (E) and transpiration (T) estimates (i.e., ERA5L, GLDAS, and MERRA2) to improve
103 the accuracy of evapotranspiration (ET) over East Asia. Li et al. (2023b) combined
104 four products, including FluxCom, Global Land Surface Satellite (GLASS) (Liang et
105 al., 2021), GLEAM, and PMLv2, to improve ET accuracy in the Nordic Region.

106 Although the above studies have demonstrated that collocation analysis can
107 effectively assess the random error variance of ET (evapotranspiration) products and
108 integrate error information from multiple data sources, these studies did not consider
109 the issue of non-zero error covariance (ECC) between different ET products. Li et al.
110 (2022) 's global ET product evaluation research revealed clear non-zero ECC
111 conditions between ERA5L and GLEAM and PMLV2 and FLUXCOM. In TC
112 analysis, non-zero ECC can result in significant biases in TC-based results (Yilmaz
113 and Crow, 2014). Furthermore, when using TC-based error information for fusion, it
114 is crucial to consider the information related to ECC, as this can help improve the
115 fusion accuracy (Dong et al., 2020b; Kim et al., 2021b).

116 In this study, we proposed a collocation-based data ensemble method, considering
117 non-zero ECC conditions, for merging multiple ET products to create the Collocation-
118 Analyzed Multi-source Ensembled Land Evapotranspiration data, abbreviated as
119 CAMELE. The second section of this paper presents the selected data information for
120 this study. In the third section, we explained the error calculation method for
121 collocation analysis and the weighted calculation method that considered ECC. The
122 fourth section analyzed the global errors of different ET products obtained through



123 these calculations and the distribution patterns of the corresponding weights. We
 124 evaluated the accuracy of the fused products and compared them with existing
 125 products using reference values from site measurements. In the fifth section, we
 126 discussed the inherent errors in the methods, analyzed the ECC between the products,
 127 and compared the differences between different fusion schemes. Finally, in the sixth
 128 section, we summarized the results obtained from this research.

129 2. Datasets

130 We selected five widely used land evapotranspiration (ET) products that spanned the
 131 period from 1980 to 2022. Furthermore, we incorporated in-situ observations to
 132 compare our merged product comprehensively. Table 1 shows the spatial and
 133 temporal resolutions of the input datasets.

134 **TABLE.1** Summary of evapotranspiration products involved.

Name	Schemes	Resolution	Period	Reference
ERA5-Land	H-TESEL	0.1°	hourly	1950-present (Muñoz-Sabater et al., 2021)
GLDAS-2	CLSM/Noah /LSM	0.25°	3-hourly	2.0: 1948-2014 (Li et al., 2019a;
			daily	2.1: 2000-present Rodell et al., 2004)
				2.2: 2003-present
GLEAM-3.7	GLEAM model	0.25°	daily	3.7a: 1980-2022 (Martens et al., 2017) 3.7b: 2003-2022
PMLv2-v017	Penman- Monteith- Leuning	0.083°	8-day average	2000-2020 (Zhang et al., 2019)
FluxCom	Machine learning	0.083°	8-day average	2001-2015 (Jung et al., 2019)



135 **2.1. ERA5-Land**

136 The European Centre for Medium-Range Weather Forecasts (ECMWF) produces the
137 latest advanced ERA5-Land dataset, referred to as ERA5L, a global hourly reanalysis
138 dataset with a spatial resolution of 0.1° . It covers the period from January 1950 until
139 approximately one week before the present (Muñoz-Sabater et al., 2021). ERA5-Land
140 is derived from the land component of the ECMWF climate reanalysis, incorporating
141 numerous improvements over previously released versions. It is based on the Tiled
142 ECMWF Scheme for Surface Exchanges over Land incorporating land surface
143 hydrology (H-TESEL), utilizing version CY45R1 of the ECMWF's Integrated
144 Forecasting System (IFS). The dataset benefits from atmospheric forcing data, which
145 acts as an indirect constraint on the model-based estimates (Hersbach et al., 2020).
146 The dataset is available through the Climate Change service of the Copernicus Center
147 at <http://cds.climate.copernicus.eu>.

148 Evapotranspiration in ERA5L, defined as "total evaporation," represents the
149 accumulated amount of water that has evaporated from the Earth's surface, including a
150 simplified representation of transpiration from vegetation into the vapor in the air.
151 The soil water and energy balance are computed using standard soil discretization.
152 Readers could consult section 8.6.5 of the IFS documentation (ECMWF, 2014). The
153 original dataset is interpolated from (1801, 3600) to (1800, 3600) using kriging
154 interpolation and then upscaled from an hourly to a daily resolution, changing spatial
155 resolution from 0.1° to 0.25° .

156 **2.2. GLDAS**

157 The Global Land Data Assimilation System (GLDAS) product utilizes advanced data
158 assimilation methodologies, integrating model and observation datasets for land-
159 surface simulations (Rodell et al., 2004). GLDAS employs multiple land-surface
160 models (LSMs), namely Noah, Mosaic, Variable Infiltration Capacity (VIC), and the



161 Community Land Model (CLM). Together, these models generate global
162 evapotranspiration estimates at fine and coarse spatial resolutions (0.01° and 0.25°)
163 and temporal resolutions (3-hourly and monthly). The most recent iteration of
164 GLDAS, version 2, consists of three components: GLDAS-2.0, GLDAS-2.1, and
165 GLDAS-2.2. GLDAS-2.0 relies entirely on the Princeton meteorological forcing input
166 data, providing a consistent temporal series from 1948 to 2014 (Sheffield et al., 2006).
167 The GLDAS-2.1 simulation commences on January 1, 2000, utilizing the conditions
168 from the GLDAS-2.0 simulation. On the other hand, GLDAS-2.2 is simulated from
169 February 1, 2003, employing the conditions from GLDAS-2.0 and forcing with
170 meteorological analysis fields from the ECMWF Integrated Forecasting System (IFS).
171 Additionally, the GRACE satellite's total terrestrial water anomaly observation is
172 assimilated into the GLDAS-2.2 product (Li et al., 2019a).

173 In this study, to cover the research period from 1980 to 2022 and address potential
174 error homogeneity issues between GLDAS-2.2 and ERA5L (both utilizing ECMWF
175 meteorological driving data), we selected GLDAS-2.0 and GLDAS-2.1 as inputs. The
176 "Evap_tavg" parameter representing evapotranspiration is derived from the original
177 products and aggregated to a daily scale. For more detailed information on the
178 GLDAS-2 models, please refer to NASA's Hydrology Data and Information Services
179 Center at <http://disc.sci.gsfc.nasa.gov/hydrology>.

180 **2.3. GLEAM**

181 The latest version of the Global Land Evaporation Amsterdam Model 3.7 (GLEAM-
182 3.7) dataset (Martens et al., 2017; Miralles et al., 2011) at 0.25° is used. This version
183 of GLEAM provides daily estimations of actual evaporation, bare soil evaporation,
184 canopy interception, transpiration from vegetation, potential evaporation, and snow
185 sublimation from 1980 to 2022. The third version of GLEAM contains a new DA
186 scheme, an updated water balance module, and evaporative stress functions. Two
187 datasets that differ only in forcing and temporal coverage are provided:



188 GLEAMv3.7a-43-year period (1980 to 2022) based on satellite and reanalysis
189 (ECMWF) data; GLEAMv3.7b-20-year period (2003 to 2022) based on only satellite
190 data. GLEAMv3.7a is used in this study. The data are freely available on the GLEAM
191 website (<https://www.gleam.eu>).

192 The cover-dependent potential evaporation rate (E_p) is calculated using the Priestley-
193 Taylor equation (Priestley and TAYLOR, 1972). Then a multiplicative stress factor is
194 used to convert E_p into actual transpiration or bare soil evaporation, which is the
195 function of microwave vegetation optimal depth (VOD) and root-zone soil moisture.
196 For detailed description, please refer to the paper by (Martens et al., 2017). The
197 GLEAM data were validated at 43 FluxNet flux sites and have been proven to provide
198 reliable AET estimations (Majozi et al., 2017).

199 **2.4. PMLv2**

200 The Penman-Monteith-Leuning version 2 global evaporation model (PMLv2) has
201 been developed based on the Penman-Monteith-Leuning model (Zhang et al., 2019;
202 Leuning et al., 2009). Initially proposed by Leuning et al. (2008), the PML model
203 underwent further enhancements by Zhang et al. (2010). The PML version 1 (PMLv1)
204 incorporates a biophysical model that considers canopy physiological processes and
205 soil evaporation to estimate surface conductance accurately (G_s), which is the focus of
206 the PM-based method. This version was subsequently enhanced by incorporating a
207 canopy conductance (G_c) model that couples vegetation transpiration with gross
208 primary productivity, resulting in the development of PML version 2 (PMLv2) as
209 described by Gan et al. (2018). Zhang et al. (2019) applied the PMLv2 model globally.
210 The daily inputs for this model include leaf area index (LAI), white sky shortwave
211 albedo, and emissivity obtained from the Moderate Resolution Imaging
212 Spectroradiometer (MODIS), as well as temperature variables (T_{max} , T_{min} , T_{avg}),
213 instantaneous variables (P_{surf} , P_a , U , q), and accumulated variables (P_{rcp} , R_{ln} , R_s)
214 from GLDAS-2.0. Evaporation is divided into direct evaporation from bare soil (E_s),



215 evaporation from solid water sources (water bodies, snow, and ice) (ET_{water}), and
216 vegetation transpiration (E_c). To ensure its accuracy, the PMLv2-ET model was
217 calibrated against 8-daily eddy covariance data from 95 global flux towers
218 representing ten different land cover types.

219 In this study, we employ the latest version, v017. The data is freely available through
220 the google earth engine [https://developers.google.com/earth-](https://developers.google.com/earth-engine/datasets/catalog/CAS_IGSNRR_PML_V2_v017)
221 [engine/datasets/catalog/CAS_IGSNRR_PML_V2_v017](https://developers.google.com/earth-engine/datasets/catalog/CAS_IGSNRR_PML_V2_v017).

222 **2.5. FluxCom**

223 FluxCom is a machine-learning-based approach combining global land-atmosphere
224 energy flux data by combining remote sensing and meteorological data (Jung et al.,
225 2019). To achieve this, FluxCom utilizes various machine-learning regression tools,
226 including tree-based methods, regression splines, neural networks, and kernel
227 methods. The outputs of FluxCom are designed based on two complementary
228 strategies: (1) FluxCom-RS, which exclusively merges remote sensing data to
229 generate high spatial resolution flux data; and (2) FluxCom-RS+METEO, which
230 combines meteorological observations with remote sensing data at a daily temporal
231 resolution. The exclusive use of remote sensing data in the ensemble allows
232 producing gridded flux products at a spatial resolution of 500m, albeit with a
233 relatively low frequency of 8 days. It is important to note that the FluxCom-RS data
234 only covers the period after 2000 due to data availability.

235 In contrast, the merging of meteorological and remote sensing data extends the
236 coverage back to 1980 at the cost of a coarser spatial resolution of 0.5° . For more
237 detailed information about the FluxCom dataset, please refer to the FluxCom website
238 (<http://FluxCom.org/>). The data is freely available upon contacting the authors.

239 In this study, we utilized the FluxCom-RS 8-daily 0.0833° energy flux data and
240 converted the latent heat values to evaporation using ERA5-Land aggregated daily air
241 temperature. Furthermore, the original evaporation data were interpolated to a spatial



242 resolution of 0.1° using the MATLAB Gaussian process regression package.

243 **2.6. Global in-situ observation: FluxNet**

244 The latest FluxNet2015 4.0 eddy-covariance data were used in our study (Pastorello et
245 al., 2020). Following the filtering process by Lin et al. (2018) and Li et al. (2019b),
246 firstly, only the measured and good-quality gap-filled data were used for quality
247 control. Secondly, we excluded days with rainfall and the subsequent day after rainy
248 events to mitigate the impact of canopy interception (Medlyn et al., 2017; Knauer et
249 al., 2018). Additionally, previous studies have indicated an energy imbalance problem
250 in FluxNet2015 data. Therefore, following the method proposed by Twine et al.
251 (2000), the measured ET data were corrected.

252 After data filtering and processing, 212 sites are selected. The selected sites are
253 distributed globally, primarily in North America and Europe. The International-
254 Geosphere–Biosphere Program (IGBP) land cover classification system (Loveland et
255 al., 1999) was employed to distinguish the 13 Plant Functional Types (PFTs) across
256 sites, including evergreen needle leaf forests (ENF, 49 sites), evergreen broadleaf
257 forests (EBF, 15 sites), deciduous broadleaf forests (DBF, 26 sites), croplands (CRO,
258 20 sites), grasslands (GRA, 39 sites), savannas (SAV, nine sites), mixed forests (MF,
259 nine sites), closed shrublands (CSH, three sites), deciduous needle leaf forests (DNF,
260 one site), open shrublands (OSH, 13 sites), snow and ice (SNO, one site), and
261 permanent wetland (WET, 21 sites).

262 **3. Method**

263 In this study, the fusion of products consisted of three steps: (1) the collocation
264 method (IVD and EIVD) was used to calculate the random error variance of the
265 selected input products, determine the regionally optimal products, and set an error
266 threshold; (2) aiming for minimum MSE, the weights of different products on each
267 grid were calculated; (3) the products were fused according to the weights to obtain a



268 long sequence of evapotranspiration products. Since IVD and EIVD were developed
269 by combining instrumental variable regression and the extended collocation system, a
270 description of TC and EC algorithms was also included.

271 **3.1. Triple collocation analysis**

272 Since its development in 1998, the implications and formulations of the triple
273 collocation problem have been investigated in many studies. Two notations are
274 proposed, based either on combinations of covariances or cross-multiplied differences
275 between inputs, denoted as difference and covariance notations (Stoffelen, 1998;
276 Dorigo et al., 2010; Su et al., 2014; McColl et al., 2014). These two notations are
277 mathematically identical under the TC-based rescaled scheme (Gruber, 2016). Here,
278 we used difference notation for demonstration.

279 The commonly used error structure for triple collocation analysis (TCA) is:

$$i = \alpha_i + \beta_i \Theta + \varepsilon_i \quad (1)$$

280 where $i \in [X, Y, Z]$ are three spatially and temporally collocated data sets; Θ is the
281 unknown true signal for relative geographical variable; α_i and β_i are additive and
282 multiplicative bias factors against the true signal, respectively; ε_i is the additive zero-
283 mean random error.

284 The above structure is also a typical instrumental variable (IV) regression. Thus, this
285 provides another perspective to introduce more variables (>3) (Dong and Crow, 2017;
286 Su et al., 2014) and polynomial models (Yilmaz and Crow, 2013; De Lannoy et al.,
287 2007) to the standard TC. We recommend that the readers refer to Su et al. (2014) for
288 a more detailed discussion on using the IV framework.

289 The basic assumptions adopted in TC are as follows: (i) Linearity between true signal
290 and data sets, (ii) signal and error stationarity, (iii) independency between random
291 error and true signal (error orthogonality), (iv) independence between random errors
292 (zero error cross-correlation, zero ECC). Although many studies have indicated that
293 some of these assumptions are often violated in practice (Li et al., 2018, 2022; Jia et



294 al., 2022), the formulation based on these assumptions is still the most robust
 295 implementation (Gruber et al., 2016b). A discussion on these assumptions will be
 296 provided in the discussion section.

297 The data sets first need to be rescaled against an arbitrary reference (e.g., X). The
 298 others are scaled through a TC-based rescaling scheme:

$$Y^X = \beta_Y^X(Y - \bar{Y}) + \bar{X} \quad Z^X = \beta_Z^X(Z - \bar{Z}) + \bar{X} \quad (2)$$

299 The overbar denotes the mean value, and β_Y^X and β_Z^X are the scaling factors as:

$$\begin{cases} \beta_Y^X = \frac{\beta_X}{\beta_Y} = \frac{\langle (X - \bar{X})(Z - \bar{Z}) \rangle}{\langle (Y - \bar{Y})(Z - \bar{Z}) \rangle} = \frac{\sigma_{XZ}}{\sigma_{YZ}} \\ \beta_Z^X = \frac{\beta_X}{\beta_Z} = \frac{\langle (X - \bar{X})(Y - \bar{Y}) \rangle}{\langle (Z - \bar{Z})(Y - \bar{Y}) \rangle} = \frac{\sigma_{XY}}{\sigma_{ZY}} \end{cases} \quad (3)$$

300 where $\langle \cdot \rangle$ is the average operator, σ_{ij} is the covariance of data sets i and j .

301 Subsequently, the error variances could be estimated by averaging the cross-
 302 multiplied data set differences as follows:

$$\begin{cases} \sigma_{\varepsilon_X}^2 = \langle (X - Y^X)(X - Z^X) \rangle \\ \sigma_{\varepsilon_Y^X}^2 = \beta_Y^{X^2} \sigma_{\varepsilon_Y}^2 = \langle (Y^X - X)(Y^X - Z^X) \rangle \\ \sigma_{\varepsilon_Z^X}^2 = \beta_Z^{X^2} \sigma_{\varepsilon_Z}^2 = \langle (Z^X - X)(Z^Y - Y^X) \rangle \end{cases} \quad (4)$$

303 Expanding the bracket and expressing the rescaling factors yields:

$$\begin{cases} \sigma_{\varepsilon_X}^2 = \sigma_X^2 - \frac{\sigma_{XY}\sigma_{XZ}}{\sigma_{YZ}} \\ \sigma_{\varepsilon_Y}^2 = \sigma_Y^2 - \frac{\sigma_{YX}\sigma_{YZ}}{\sigma_{XZ}} \\ \sigma_{\varepsilon_Z}^2 = \sigma_Z^2 - \frac{\sigma_{ZX}\sigma_{ZY}}{\sigma_{XY}} \end{cases} \quad (5)$$

304 When selecting various scaling references, it is essential to note that the absolute error
 305 variances remain consistent. However, this choice can have an impact on the
 306 estimation of data sensitivity to the actual signal ($\beta_i^2 \sigma_\theta^2$), which serves as a crucial
 307 indicator for comparing spatial error patterns. In order to address the reliance on a
 308 specific scaling reference, Draper et al. (2013) introduced the fractional root-mean-
 309 squared-error ($fMSE_i$). This measure is obtained by normalizing the unscaled error



310 variance with respect to the true signal variance:

$$fMSE_i = \frac{\sigma_{\varepsilon_i}^2}{\sigma_i^2} = \frac{\sigma_{\varepsilon_i}^2}{\beta_i^2 \sigma_{\Theta}^2 + \sigma_{\varepsilon_i}^2} = \frac{1}{1 + SNR_i} \quad (6)$$

311 where $SNR_i = \frac{\beta_i^2 \sigma_{\Theta}^2}{\sigma_{\varepsilon_i}^2} \in [0,1]$ is the normalized signal-to-noise ratio. $SNR = 0$

312 indicates a noise-free observation, while $SNR = 1$ corresponds that the variances of
 313 estimates equal that of the true signal.

314 Following similar ideas, Mccoll et al. (2014) extended the framework to estimate the
 315 data-truth correlation, known as extended triple collocation (ETC):

$$R_i^2 = \frac{\beta_i^2 \sigma_{\Theta}^2}{\beta_i^2 \sigma_{\Theta}^2 + \sigma_{\varepsilon_i}^2} = \frac{SNR_i}{1 + SNR_i} = \frac{1}{1 + NSR_i} \quad (7)$$

$$R_i^2 = 1 - fMSE_i$$

316 In comparison to the conventional coefficient of determination R_{ij} , which is
 317 influenced by data noise and sensitivity. It is important to note that R_i^2 is merely based
 318 on the data set i , whereas R_{ij} is influenced by both data set i and reference j . In other
 319 words, R_i^2 incorporates the dependency on the chosen reference. Thus, TC-derived
 320 $fMSE_i$ and R_i^2 serve as superior indicators for assessing the actual quality of data, as
 321 discussed by Kim et al. (2021b) and Gruber et al. (2020).

322 3.2. Double instrumental variable technique

323 The assumed error structure in TC is also a typical instrumental variable (IV)
 324 regression. In practical usage, finding three completely independent sets of products is
 325 usually tricky. Su et al. (2014) effectively improve the applicability of the TC method
 326 by using the lag-1 time series (e.g., $X_{t-1} = \alpha_X + \beta_X \Theta_{t-1} + \varepsilon_{X,t-1}$) from one of the
 327 two sets of data as the third input for TC. In this way, we only need two independent
 328 products for input.

329 Such process includes another assumption that all data sets contain serially white
 330 errors (i.e., $\langle \varepsilon_{i,t} \varepsilon_{i,t-1} \rangle = 0$, zero auto-correlation). Building upon this, Dong et al.
 331 (2019) utilizes the lag-1 time series from both data sets as inputs and propose a more



332 stable double instrumental variable (IVD) method.

333 For a double input $[X, Y$ with $\sigma_{\varepsilon_X \varepsilon_Y} = 0]$, the linear error model and related lag-1
 334 time series can be expressed as:

$$\begin{cases} X = \alpha_X + \beta_X \Theta + \varepsilon_X & I = \alpha_X + \beta_X \Theta_{t-1} + \varepsilon_{X_{t-1}} \\ Y = \alpha_Y + \beta_Y \Theta + \varepsilon_Y & J = \alpha_Y + \beta_Y \Theta_{t-1} + \varepsilon_{Y_{t-1}} \end{cases} \quad (8)$$

335 where I and J are the lag-1 time series of X and Y , respectively.

336 Assuming product errors are mutually independent and orthogonal to the truth, the
 337 covariance between the products is expressed as:

$$\begin{cases} \sigma_X^2 = \beta_X^2 \sigma_\Theta^2 + \sigma_{\varepsilon_X}^2 & \sigma_Y^2 = \beta_Y^2 \sigma_\Theta^2 + \sigma_{\varepsilon_Y}^2 \\ \sigma_{XY} = \beta_X \beta_Y \sigma_\Theta^2 \\ \sigma_{IX} = \beta_X^2 L_{\Theta\Theta} & \sigma_{JY} = \beta_Y^2 L_{\Theta\Theta} \end{cases} \quad (9)$$

338 where $L_{ii} = \langle i_t i_{t-1} \rangle$ is the auto-covariance. Therefore, the IVD-estimated dynamic
 339 range ratio scaling factors yields:

$$s_{ivd} \equiv \frac{\beta_X}{\beta_Y} = \sqrt{\frac{\sigma_{IX}}{\sigma_{JY}}} \quad (10)$$

340 Hence, the random error variances of X and Y can be solved as:

$$\begin{cases} \sigma_{\varepsilon_X}^2 = \sigma_X^2 - \sigma_{XY} * s_{ivd} \\ \sigma_{\varepsilon_Y}^2 = \sigma_Y^2 - \frac{\sigma_{XY}}{s_{ivd}} \end{cases} \quad (11)$$

341 3.3. Extended instrumental variable technique

342 Furthermore, by adopting the designed matrix in extended collocation (EC) (Gruber et
 343 al., 2016a), Dong et al. (2020a) present the extended double instrumental variable
 344 technique (denoted as EIVD) to estimate the error variance matrix with only two
 345 independent data sets.

346 For a triplet input $[i, j, k$ with $\sigma_{\varepsilon_i \varepsilon_j} \neq 0]$. The dynamic range ratio scaling factors can
 347 be estimated as follows:



$$s_{ij} \equiv \frac{\beta_i}{\beta_j} = \sqrt{\frac{L_{ii}}{L_{jj}}} \quad (12)$$

348 where $L_{ii} = \langle i_t i_{t-1} \rangle$ is the auto-covariance of inputs. Subsequently, the sensitivity
 349 and absolute error variance of the data set follow:

$$\beta_j^2 \sigma_{\Theta}^2 = \sigma_{ij} \sqrt{\frac{L_{ii}}{L_{jj}}} \quad \sigma_{\varepsilon_j}^2 = \sigma_{ij} \sqrt{\frac{L_{ii}}{L_{jj}}} - \sigma_i^2 \quad (13)$$

350 The cross-multiplied factors can be estimated by:

$$\beta_i \beta_j \sigma_{\Theta}^2 = \sigma_{ik} \sqrt{\frac{L_{jj}}{L_{kk}}} = \sigma_{jk} \sqrt{\frac{L_{ii}}{L_{kk}}} \quad \sigma_{\varepsilon_i \varepsilon_j} = \sigma_{ij} - \beta_i \beta_j \sigma_{\Theta}^2 \quad (14)$$

351 Hence, for a triplet with the input of $[X, Y, Z]$ with $\sigma_{\varepsilon_X \varepsilon_Y} \neq 0$: the matrix notation of
 352 the above system with $\mathbf{y} = \mathbf{A}\mathbf{x}$ is given as:

$$\mathbf{y} = \begin{pmatrix} \sigma_X^2 \\ \sigma_Y^2 \\ \sigma_Z^2 \\ \sigma_{XY} \\ \sigma_{XZ} \sqrt{\frac{L_{XX}}{L_{ZZ}}} \\ \sigma_{YZ} \sqrt{\frac{L_{YY}}{L_{ZZ}}} \\ \sigma_{ZX} \sqrt{\frac{L_{ZZ}}{L_{XX}}} \\ \sigma_{ZY} \sqrt{\frac{L_{ZZ}}{L_{YY}}} \\ \sigma_{XZ} \sqrt{\frac{L_{YY}}{L_{ZZ}}} \\ \sigma_{YZ} \sqrt{\frac{L_{XX}}{L_{ZZ}}} \end{pmatrix}_{10 \times 1} \quad \mathbf{A} = \begin{pmatrix} \mathbf{I}_{4 \times 4} & \mathbf{I}_{4 \times 4} \\ \begin{pmatrix} 1 & 0 & 0 & 0 \\ 0 & 1 & 0 & 0 \\ 0 & 0 & 1 & 0 \\ 0 & 0 & 1 & 0 \\ 0 & 0 & 0 & 1 \\ 0 & 0 & 0 & 1 \end{pmatrix}_{6 \times 4} & \mathbf{0}_{6 \times 4} \end{pmatrix}_{10 \times 8} \quad \mathbf{x} = \begin{pmatrix} \beta_X^2 \sigma_{\Theta}^2 \\ \beta_Y^2 \sigma_{\Theta}^2 \\ \beta_Z^2 \sigma_{\Theta}^2 \\ \beta_X \beta_Y \sigma_{\Theta}^2 \\ \sigma_{\varepsilon_X}^2 \\ \sigma_{\varepsilon_Y}^2 \\ \sigma_{\varepsilon_Z}^2 \\ \sigma_{\varepsilon_X \varepsilon_Y} \end{pmatrix}_{8 \times 1} \quad (15)$$

353 Likewise, the least-squared solution for unknown \mathbf{x} is then solved by:

$$\mathbf{x} = (\mathbf{A}^T \mathbf{A})^{-1} \mathbf{A}^T \mathbf{y} \quad (16)$$



354 3.4. Weight Estimation

355 Our objective is to predict an uncertain variable, such as evapotranspiration (ET) over
 356 time at a specific location, by utilizing parent products that may contain random errors.
 357 The underlying concept of weighted averaging is to extract independent information
 358 from multiple data sources to enhance prediction accuracy by mitigating the effects of
 359 random errors. The effectiveness of this approach relies on the independence of the
 360 individual data sources under consideration. Weighted averaging has found
 361 applications in various fields following the influential work of Bates and Granger
 362 (1969), who proposed the optimal combination of forecasts based on a mean square
 363 error (MSE) criterion. In this context, the term "optimal" refers to minimizing the
 364 variance of residual random errors in the least squares sense. Mathematically, this
 365 weighted average can be expressed as follows:

$$\bar{x} = \bar{\mathbf{W}}^T \bar{\mathbf{X}} = \sum_{i=1}^N \omega_i x_i \quad (17)$$

366 where \bar{x} is the merged estimate; $\bar{\mathbf{X}} = [x_1, \dots, x_n]^T$ contains the temporally collocated
 367 estimates from N different parent products, which are merged with relative zero-mean
 368 random error $\bar{\mathbf{e}} = [\varepsilon_1, \dots, \varepsilon_n]^T$; and $\bar{\mathbf{W}} = [\omega_1, \dots, \omega_n]^T$ contains the weights assigned
 369 to these estimates, where $\omega_i \in [0,1]$ and $\sum \omega_i = 1$ ensuring an unbiased prediction.

370 The averaging weights can be expressed as the solution to the problem:

$$\min f(\bar{\mathbf{W}}) = \mathbb{E}(\bar{\mathbf{e}}^T \bar{\mathbf{W}})^2 \quad (18)$$

371 where $\mathbb{E}()$ is the operator for mathematical expectation, the solution of this problem is
 372 determined by the individual random error characteristics of the input data sets and
 373 can be derived from their covariance matrix (Bates and Granger, 1969; Gruber et al.,
 374 2017; Kim et al., 2021b):

$$\begin{aligned} \bar{\mathbf{W}} &= (\bar{\mathbf{I}}^T \mathbb{E}(\bar{\mathbf{e}} \bar{\mathbf{e}}^T) \bar{\mathbf{I}})^{-1} \mathbb{E}(\bar{\mathbf{e}} \bar{\mathbf{e}}^T) \bar{\mathbf{I}} \\ \sigma_{\bar{x}}^2 &= (\bar{\mathbf{I}}^T \mathbb{E}(\bar{\mathbf{e}} \bar{\mathbf{e}}^T) \bar{\mathbf{I}})^{-1} \end{aligned} \quad (19)$$

375 where $\mathbb{E}(\bar{\mathbf{e}} \bar{\mathbf{e}}^T)$ is the $N \times N$ error covariance matrix that holds the random error



376 variance $\sigma_{\varepsilon_i}^2$ of the parent products in the diagonals and relative error covariances $\sigma_{\varepsilon_i \varepsilon_j}$
 377 in the off-diagonals; $\vec{\mathbf{1}} = [1, \dots, 1]^T$ is an ones-vector of length N ; and $\sigma_{\varepsilon_{\bar{x}}}^2$ is the
 378 resulting random error variances of the merged estimate.
 379 When only two groups of products are used as input ($N = 2$), it is generally assumed
 380 that the errors between them are independent. In this case, the weights are as follows:

$$\mathbb{E}(\vec{\mathbf{e}}\vec{\mathbf{e}}^T) = \begin{bmatrix} \sigma_{\varepsilon_1}^2 & 0 \\ 0 & \sigma_{\varepsilon_2}^2 \end{bmatrix} \quad (20)$$

$$\omega_1 = \frac{\sigma_{\varepsilon_2}^2}{\sigma_{\varepsilon_1}^2 + \sigma_{\varepsilon_2}^2} \quad \omega_2 = \frac{\sigma_{\varepsilon_1}^2}{\sigma_{\varepsilon_1}^2 + \sigma_{\varepsilon_2}^2}$$

381 In most cases, we can identify three sets of products as inputs ($N = 3$). In this
 382 scenario, we consider the possibility of error homogeneity, assuming a non-zero ECC
 383 exists between inputs 1 and 2. In this case, the error matrix can be represented as:

$$\mathbb{E}(\vec{\mathbf{e}}\vec{\mathbf{e}}^T) = \begin{bmatrix} \sigma_{\varepsilon_1}^2 & \sigma_{\varepsilon_1 \varepsilon_2} & 0 \\ \sigma_{\varepsilon_1 \varepsilon_2} & \sigma_{\varepsilon_2}^2 & 0 \\ 0 & 0 & \sigma_{\varepsilon_3}^2 \end{bmatrix} \quad (21)$$

384 The weights can then be written as:

$$\vec{\mathbf{W}} = \begin{cases} \frac{\sigma_{\varepsilon_2}^2 - \sigma_{\varepsilon_1 \varepsilon_2}}{(\sigma_{\varepsilon_1}^2 \sigma_{\varepsilon_2}^2 - \sigma_{\varepsilon_1 \varepsilon_2}^2) * \mathbb{Z}} \\ \frac{\sigma_{\varepsilon_1}^2 - \sigma_{\varepsilon_1 \varepsilon_2}}{(\sigma_{\varepsilon_1}^2 \sigma_{\varepsilon_2}^2 - \sigma_{\varepsilon_1 \varepsilon_2}^2) * \mathbb{Z}} \\ \frac{1}{\sigma_{\varepsilon_3}^2 * \mathbb{Z}} \end{cases} \quad (22)$$

$$\mathbb{Z} = \frac{\sigma_{\varepsilon_1}^2 + \sigma_{\varepsilon_2}^2 - 2\sigma_{\varepsilon_1 \varepsilon_2}}{\sigma_{\varepsilon_1}^2 \sigma_{\varepsilon_2}^2 - \sigma_{\varepsilon_1 \varepsilon_2}^2} + \frac{1}{\sigma_{\varepsilon_3}^2}$$

385 It is essential to acknowledge that before applying these weights for merging the data
 386 sets, it is necessary to address any existing systematic differences. Typically, this is
 387 achieved by rescaling the data sets to a standardized data space. Consequently, the
 388 weights can be derived from the rescaled data sets using Eq (2)-(3) and converge
 389 accordingly. This procedure ensures the accuracy and reliability of the merged data
 390 sets for further analysis.



391 If ECC is not considered (i.e., setting $\sigma_{\varepsilon_1\varepsilon_2} = 0$), Eq (22) represents the weight
392 calculation method commonly used in most TC fusion studies. This method was
393 initially applied by Yilmaz et al.(2012) in the fusion of multi-source soil moisture
394 products and later improved by Gruber et al. (2017) and further applied in the
395 production of the ESA CCI global soil moisture product (Gruber et al., 2019). Dong et
396 al. (2020b) also adopted this approach to fusing multi-source precipitation products.
397 In the study of evapotranspiration, Li et al. (2023b) and Park et al.(2023) utilized a
398 weight calculation method that does not consider non-zero ECC and fused multiple
399 ET products in the Nordic and East Asia, respectively, achieving satisfactory fusion
400 results.

401 In contrast to the fusion studies mentioned above for evapotranspiration products, for
402 the first time, the consideration of non-zero ECC is incorporated into the fusion
403 process and integrated into the weight calculation. Yilmaz and Crow (2014) have
404 demonstrated that TC underestimates error variances when the zero ECC assumption
405 is violated. Li et al. (2022), in their evaluation study of global ET products using the
406 collocation method, also indicated the existence of error homogeneity issues between
407 commonly used ET products (such as ERA5L and GLEAM), necessitating the
408 consideration of the influence of non-zero ECC. The merging technique employed in
409 this study provides a more explicit characterization of product errors and facilitates
410 the derivation of more reliable weight coefficients, thereby achieving superior fusion
411 outcomes.

412 The differences in results are evaluated at the site scale by contrasting the scenarios
413 without considering non-zero ECC and directly using simple averages to compare and
414 validate the advantages of the weight calculation method used in our study.

415 **3.5. Merging combination**

416 In this study, we employ five commonly used global land surface evapotranspiration
417 (ET) products as described in the datasets section. PMLv2 and FluxCom have an



418 original resolution of 0.083° and an 8-day average. In this research, they are
419 interpolated to 0.1° resolution, and the values for each data period of 8 days are kept
420 consistent. For example, the values for March 5 to March 12, 2000, are the same. This
421 operation is performed to ensure adequate data for the collocation analysis (Kim et al.,
422 2021a), and any potential errors resulting from it will be discussed in the discussion
423 section.

424 As mentioned in the methodology section, it is vital to consider the issue of random
425 error homogeneity among different products before applying the collocation method.
426 Although EC or EIVD methods can be used to calculate the ECC between specific
427 pairs of products, it is necessary to determine which pairs of products have non-zero
428 ECC conditions. In previous research, Li et al.(2022) employed five collocation
429 methods (IVS/IVD/TC/EIVD/EC) to analyze the performance of five sets of ET
430 products (ERA5L/GLEAMv3/PMLv2/FluxCom/PMLv2) at the global scale, and
431 applied EC and EIVD methods to calculate the ECC between different products. The
432 results indicated a relatively significant error homogeneity between PMLv2 and
433 FluxCom at a resolution of 0.1° (with a global average ECC of approximately 0.3).
434 The error homogeneity could be attributed to both products utilizing GLDAS
435 meteorological data as input, despite their different methods for ET estimation. At a
436 resolution of 0.25° , ERA5L and GLEAM exhibited a more apparent error correlation
437 (with a global average ECC of approximately 0.4). Considering the long temporal
438 data of GLEAMv3 version a, ECMWF meteorological data was chosen as the driving
439 force, making the error correlation between the two products predictable.

440 Therefore, this study assumes that non-zero ECC situations occur between PMLv2-
441 FluxCom and ERA5L-GLEAM. We also calculated the possible ECC situations
442 among other products, presented in the discussion section and the appendix. Based on
443 the analysis, our assumed non-zero ECC situations align reasonably well with the
444 actual circumstances.

445 In addition, previous research suggests that the IVD method outperforms the IVS



446 method in scenarios involving two sets of inputs, while the EIVD method is
447 considered more reliable than the TC method in situations with three sets of inputs (Li
448 et al., 2022; Kim et al., 2021a). Therefore, in this study, the IVD and EIVD methods
449 are selected for computation based on different combinations of inputs. Table 2
450 presents the data and methods used during corresponding periods. When only two sets
451 of products are available, we employ the IVD method for fusion and calculate weights
452 using Eq. (20). When three sets of products are available, we utilize the EIVD method
453 for fusion and calculate weights using Eq. (22).

454 **TABLE.2** Combination of inputs and accessible methods

Scenario 1 (0.1°)		
Period	Selected Inputs	Method
(2000.02.26-2000.12.31)	ERA5L/ PMLv2	IVD
(2001.01.01-2015.12.27)	ERA5L/ FluxCom/ PMLv2	EIVD
(2015.12.28-2020.12.26)	ERA5L/ PMLv2	IVD
Scenario 2 (0.25°)		
Period	Selected Inputs	Method
(1980.01.01-1999.12.31)	ERA5L/ GLDAS20/ GLEAMv3.7a	EIVD
(2000.01.01-2022.12.31)	ERA5L/ GLDAS21/ GLEAMv3.7a	

455 It should be noted that the same product can have different versions. In this study,
456 appropriate versions are selected based on the following principles: (1) Selection
457 based on the corresponding data coverage duration; (2) Choosing the latest version
458 while considering the assumption of non-zero ECC conditions; (3) Making efforts to
459 select the exact product versions for different periods, to avoid uncertainties caused
460 by version changes. We selected a subset of sites to compare the fusion results using
461 different versions, and the corresponding details will be presented in the discussion
462 section.

463 3.6. Evaluation indices

464 Five statistical indicators, namely Root-mean-squared-error (*RMSE*), Pearson's



465 correlation coefficient (R), Mean-absolute-error (MAE), unbiased $RMSE$ ($ubRMSE$)
 466 and Kling-Gupta Efficiency (KGE), are selected for comparison with existing
 467 products. The relative equations are shown as follows:

$$RMSE = \sqrt{\frac{\sum_{i=1}^n (sim_i - obs_i)^2}{n}} \quad (23)$$

$$R = \frac{\sum_{i=1}^n (sim_i - \overline{sim})(obs_i - \overline{obs})}{\sqrt{\sum_{i=1}^n (sim_i - \overline{sim})^2 \sum_{i=1}^n (obs_i - \overline{obs})^2}} \quad (24)$$

$$-1 \leq R \leq 1$$

$$MAE = \frac{1}{n} \sum_{i=1}^n |sim_i - obs_i| \quad (25)$$

$$ubRMSE = \sqrt{\frac{\sum_{i=1}^n \left[\frac{(sim_i - \overline{sim})}{n} - (obs_i - \overline{obs}) \right]^2}{n}} \quad (26)$$

468 Where sim is the simulations, obs is the observation as reference.
 469 The KGE (Gupta et al., 2009) addressed several shortcomings in Nash-Sutcliffe
 470 Efficiency (NSE) and are increasingly used for calibration and evaluation (Knoben et
 471 al., 2019), given by:

$$KGE = 1 - \sqrt{(r - 1)^2 + \left(\frac{\sigma_{sim}}{\sigma_{obs}} - 1\right)^2 + \left(\frac{\mu_{sim}}{\mu_{obs}} - 1\right)^2} \quad (27)$$

472 Where σ_{obs} and σ_{sim} are the standard deviations of observations and simulations;
 473 μ_{obs} and μ_{sim} are the mean of observations and simulations. Similar to NSE , $KGE = 1$
 474 indicates perfect agreement of simulations, while $KGE < 0$ reveals that the average of
 475 observations is better than simulations (Towner et al., 2019).

476 4. Results

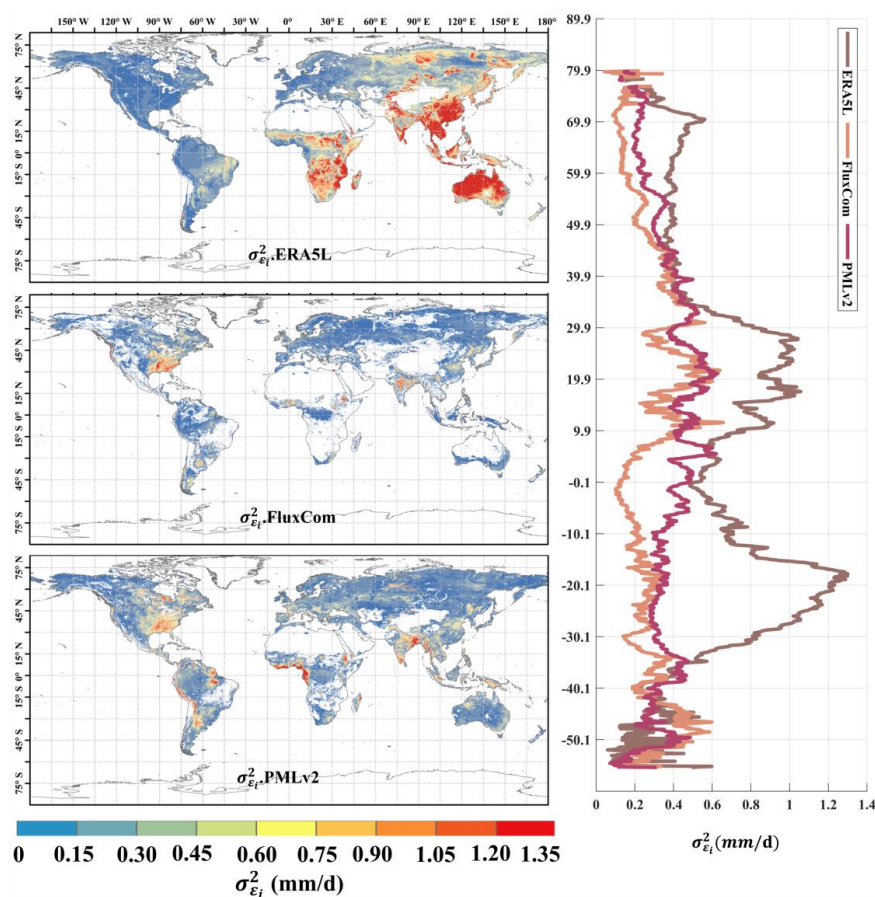
477 In this study, we aimed to compare and evaluate the performance of fused products at
 478 both site and global scales. Specifically, Lu et al. (2021) 's global 0.25° daily-scale ET
 479 product derived using Reliability Ensemble Averaging (denoted as REA) was also
 480 selected for comparative analysis. At the site scale, the performance of the fused



481 products was evaluated against 212 FluxNet observations and compared with other
482 products, including the simple average. At the global scale, the mean and temporal
483 variations of the land surface ET calculated by the fused products were compared
484 with those of other products.

485 4.1. Analysis of error variances

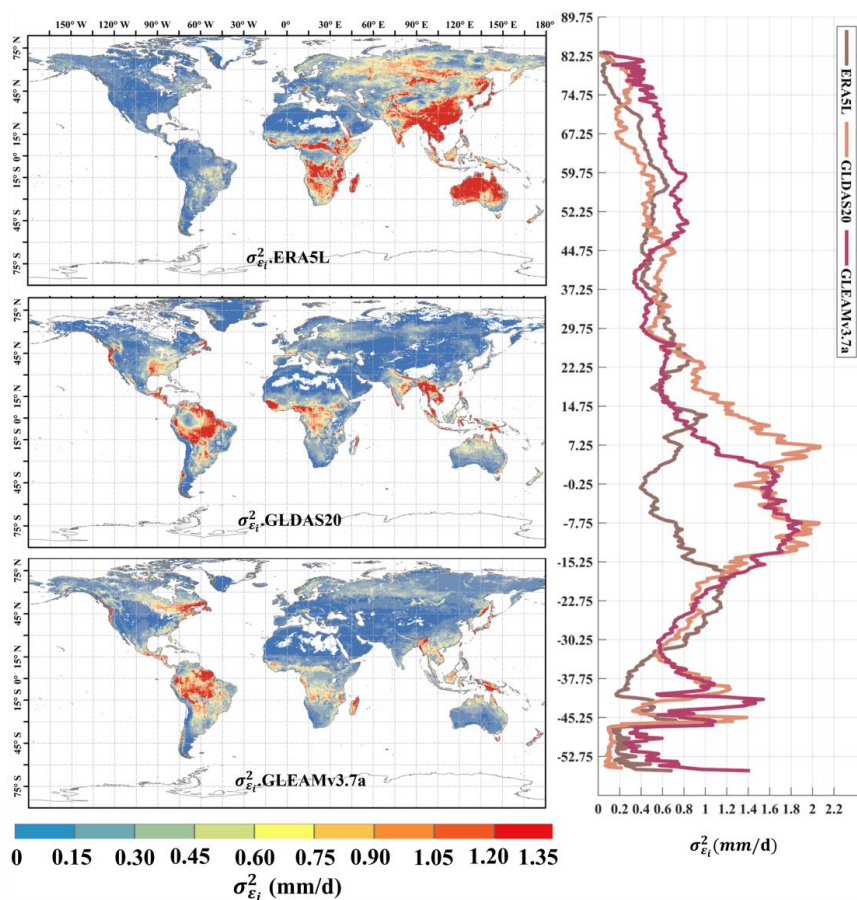
486 This section analyzed the random error variances of the 0.1° and 0.25° inputs obtained
487 using the EIVD method.



488
489 **FIGURE.1** Global distribution of absolute error variances ($\sigma_{\epsilon_i}^2$) of ERA5L, FluxCom,
490 and PMLv2 using EIVD at 0.1° from 2001 to 2015, depicted alongside corresponding
491 variation curves of average with latitude.



492 Figure 1 represents the random errors of the correlation products calculated using the
493 EIVD method from 2001 to 2015 at 0.1° , where a non-zero ECC is assumed between
494 FluxCom and PMLv2. The areas with missing values are due to the absence of data
495 from either FluxCom or PMLv2 in those regions. The global random error variances
496 (mean \pm standard deviation) obtained using the EIVD method are as follows: ERA5L:
497 0.58 ± 0.53 mm/day, FluxCom: 0.12 ± 0.13 mm/day, PMLv2: 0.17 ± 0.14 mm/day.
498 These results indicate that FluxCom performs best overall, while ERA5L performs the
499 poorest. Regarding spatial distribution, regions with more significant random errors in
500 ERA5L are mainly located in East Asia, Australia, and southern Africa. On the other
501 hand, FluxCom and PMLv2 show relatively more considerable uncertainties in the
502 southeastern United States. The latitude distribution reveals that ERA5L has the
503 highest uncertainty, primarily in the vicinity of 20° to 30° north and south, consistent
504 with its spatial distribution.



505

506

507

508

509

510

511

512

513

514

515

516

FIGURE.2 Global distribution of absolute error variances ($\sigma_{\epsilon_i}^2$) of ERA5L,

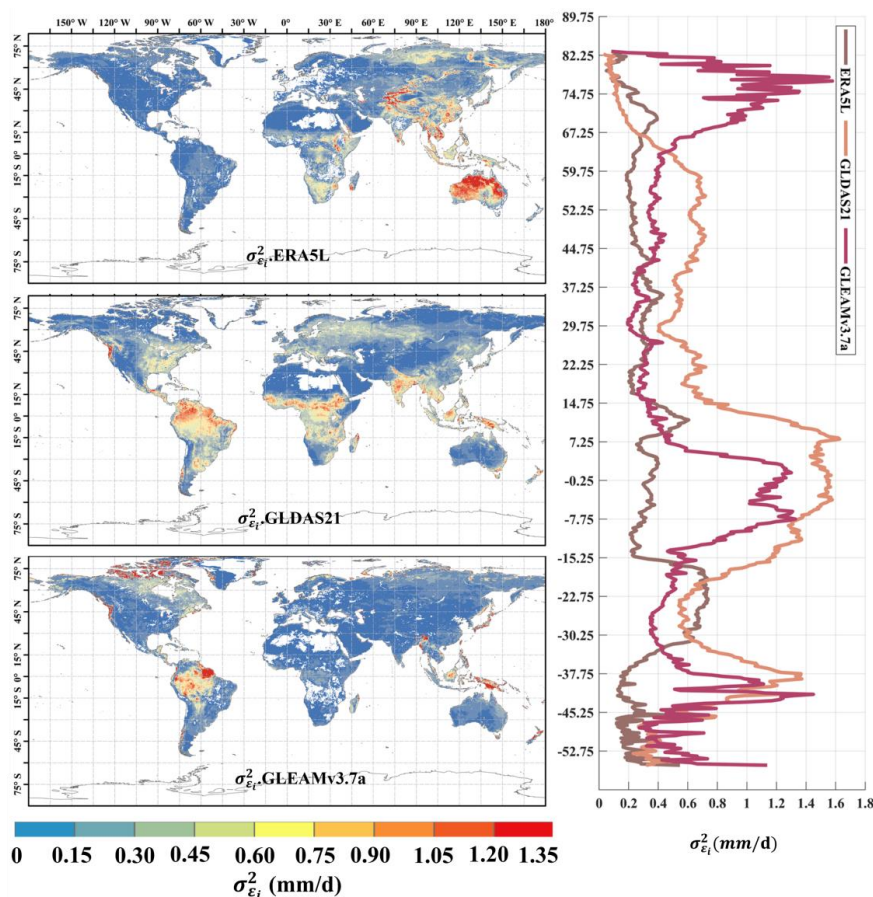
GLDAS2.0, and GLEAMv3.7a using EIVD at 0.25° from 1980 to 1999, depicted

alongside corresponding variation curves of average with latitude.

The distribution of random error variance for ERA5L (0.59 ± 0.58 mm/d), GLDAS2.0 (0.37 ± 0.44 mm/d), and GLEAMv3.7a (0.38 ± 0.36 mm/d) from 1980 to 1999 at 0.25° is shown in Figure 2. Here, we assumed a non-zero ECC between ERA5L and GLEAM. The ERA5L data was resampled from a 0.1° resolution to 0.25° , and its error distribution pattern is like that of the 0.1° resolution. It exhibits higher uncertainties in East Asia, Australia, and southern Africa. GLDAS and GLEAM exhibit relatively higher uncertainty over the southeastern United States and the Amazon Plain. GLDAS and GLEAM show similar performance among the three



517 products, while ERA5L performs relatively worse. Regarding the average distribution
 518 with latitude, ERA5L demonstrates a more even distribution, whereas GLDAS and
 519 GLEAM exhibit relatively higher uncertainties in tropical regions.



520
 521 **FIGURE.3** Global distribution of absolute error variances ($\sigma_{\epsilon_i}^2$) of ERA5L,
 522 GLDAS2.1, and GLEAMv3.7a using EIVD at 0.25° from 2000 to 2022, depicted
 523 alongside corresponding variation curves of average with latitude.
 524 In addition, Figure 3 presents the distribution of random error variance for ERA5L
 525 (0.32 ± 0.33 mm/d), GLDAS2.1 (0.35 ± 0.29 mm/d), and GLEAMv3.7a (0.38 ± 0.36
 526 mm/d) from 2000 to 2022 at a resolution of 0.25° . The non-zero ECC assumption was
 527 made between ERA5L and GLEAM. In this combination, ERA5L shows significantly
 528 lower errors than in previous periods, indicating improved ERA5L performance



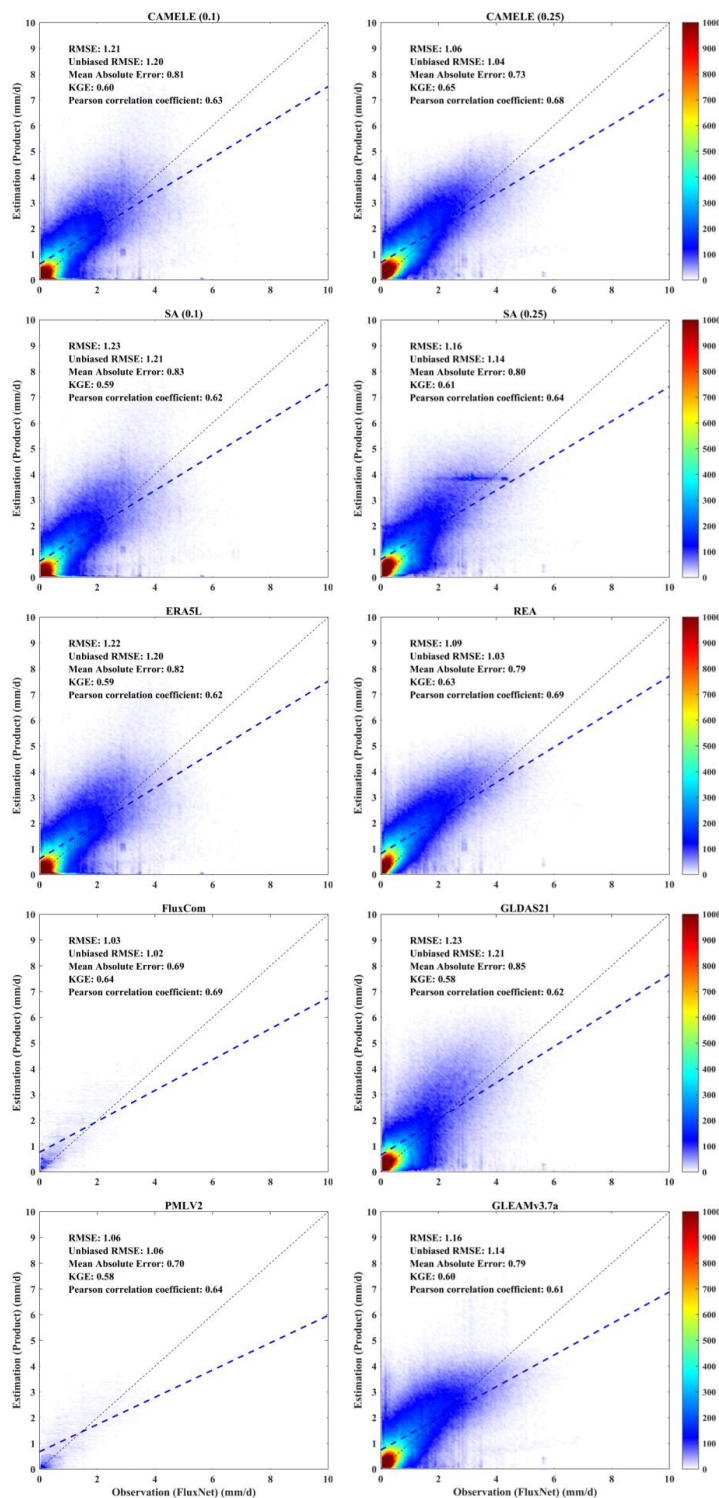
529 during this time frame. However, ERA5L still exhibits more significant errors in the
530 East Asia and Australia regions compared to the other two datasets. The overall errors
531 for GLDAS and GLEAM have also decreased, but there are still random error
532 variances exceeding 1.0 mm/d in the Amazon plain and Indonesia region. Regarding
533 the latitudinal distribution, ERA5L shows relatively smooth changes, while GLDAS
534 and GLEAM exhibit similar trends. However, GLEAM demonstrates a noticeable
535 increase in errors near the Arctic.

536 For the analysis at a resolution of 0.1° , we also applied the IVD method to calculate
537 the errors between ERA5L and PMLv2 for two time periods: 2000 and 2015 to 2020.
538 Since the analysis of product errors is not the focus of this paper, we provide the
539 results of the IVD in the appendix. Grids with higher random error variances
540 correspond to smaller weights when calculating the weights. The weight distribution
541 calculated at different time intervals is available in the appendix.

542 **4.2. Site-scale evaluation and comparison**

543 At the site scale, the performance of CAMELE was compared with FluxNet as the
544 reference. In this subsection, Figure 4 and Table 3 correspond to each other, as they
545 integrate data from 212 sites for all available periods, allowing for a comparative
546 analysis of the performance of different products at different times. Similarly, Figure
547 5 and Table 4 correspond to each other, where different product metrics were
548 calculated for each site, and the calculated metric results were subjected to statistical
549 analysis.

550





552 **FIGURE.4** Scatter plots of product corresponding to the available period data from
 553 212 FluxNet sites. The colorbar represents the density, with darker colors indicating
 554 higher concentration. The left and right columns present results for 0.1° and 0.25°
 555 resolutions, respectively, with "SA" indicating the results for simple average.

556 Relevant statistical metrics are annotated in their respective figures.
 557 The scatter plots in Figure 4 show that CAMELE performed well at both 0.1° and
 558 0.25° resolutions. At 0.1° resolution, FluxCom and PMLv2 had fewer data points due
 559 to their original product being based on an 8-day average resolution, but overall, they
 560 showed the best performance. CAMELE exhibited a performance at a station scale
 561 like ERA5L. At 0.25° resolution, CAMELE performed similarly to the other datasets,
 562 with reasonable accuracy. Notably, there was an improvement in the KGE and R
 563 indices. The fitted line was closer to the 1:1 line, indicating a closer agreement with
 564 the observed values. Interestingly, the results obtained from the simple average were
 565 also acceptable, but SA (0.25°) had a large concentration of data points between (2-4
 566 mm/d), which might be attributed to the inputs having a high concentration within that
 567 range. Theoretically, the simple average assumes that each product performs equally
 568 on each grid cell, which does not align with the actual situation.

569 **Table.3** Average values of different metrics for CAMELE and other fusion schemes
 570 corresponding to the available period data from 212 FluxNet sites. The bolded
 571 sections indicate the schemes with the best performance in their respective metrics.

	Product	RMSE (mm/d)	ubRMSE (mm/d)	MAE (mm/d)	KGE	R
0.1°-daily	CAMELE	1.21	1.20	0.81	0.60	0.63
	SA	1.23	1.21	0.83	0.59	0.62
	ERA5L	1.22	1.20	0.82	0.59	0.62
	FluxCom	1.03	1.02	0.69	0.64	0.69
	PMLv2	1.06	1.06	0.70	0.58	0.64
0.25°-daily	CAMELE	1.06	1.04	0.73	0.65	0.68
	SA	1.16	1.14	0.80	0.61	0.64
	REA	1.09	1.03	0.79	0.63	0.69



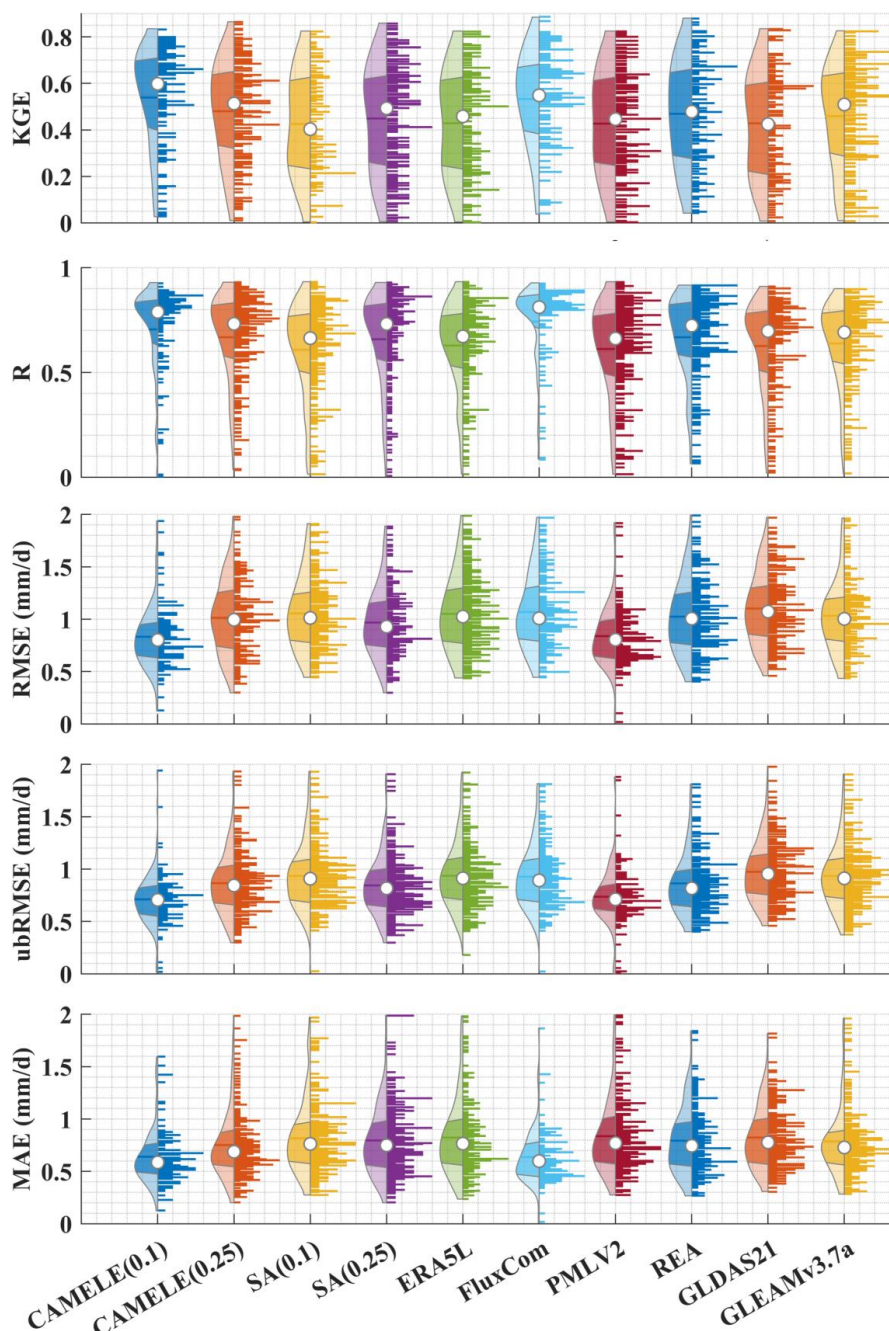
GLDAS21	1.23	1.21	0.85	0.58	0.62
GLEAMv3.7a	1.16	1.14	0.79	0.60	0.61

572 The information in Table 3 corresponds to Figure 4 and presents the results of various
573 product indicators. The bolded parts indicate the products with the best corresponding
574 indicators. The results indicate that CAMELE performed well at both 0.1° and 0.25°
575 resolutions, mainly showing improvements in the KGE and R indicators. FluxCom
576 exhibited the best performance; however, considering that this product utilized
577 FluxNet sites for result calibration, this phenomenon is reasonable. In this study, we
578 pooled the data from all 212 available periods at the stations as a reference without
579 considering the differences between individual sites. This approach provided an initial
580 validation of the reliability of CAMELE at all sites.

581 The information in Figure 5 corresponds to the data presented in Table 4, which
582 involves the calculation of five indicators at each site, followed by statistical analysis
583 of these indicators. From the distribution of the violin plots, it can be observed that a
584 violin plot with a closer belly to 1 indicates better results in terms of the R and KGE
585 indicators. CAMELE performs exceptionally well overall, closely resembling PMLv2
586 and FluxCom. On the other hand, the results obtained from Simple Average are
587 relatively poorer. Regarding the RMSE, ubRMSE, and MAE indicators, a violin plot
588 with a closer belly to 0 suggests more minor errors. CAMELE shows a significant
589 improvement in performance at the 0.1° level. This indicates that the fusion method
590 effectively reduces errors, aligning with the original intention of weight calculation.

591 Additionally, FluxCom and PMLv2 also exhibit minimal errors, which is expected
592 considering their utilization of FluxNet sites for error correction. Furthermore, SA
593 shows significantly larger errors. Although the simple average method can
594 compensate for positive and negative errors between inputs in some instances, it can
595 also lead to error accumulation, as evidenced by the results in the violin plots.

596



597

598

599

Figure.5 Violin plots obtained by aggregating five different statistical indicators, calculated separately for each site. In each violin plot, the left side represents the

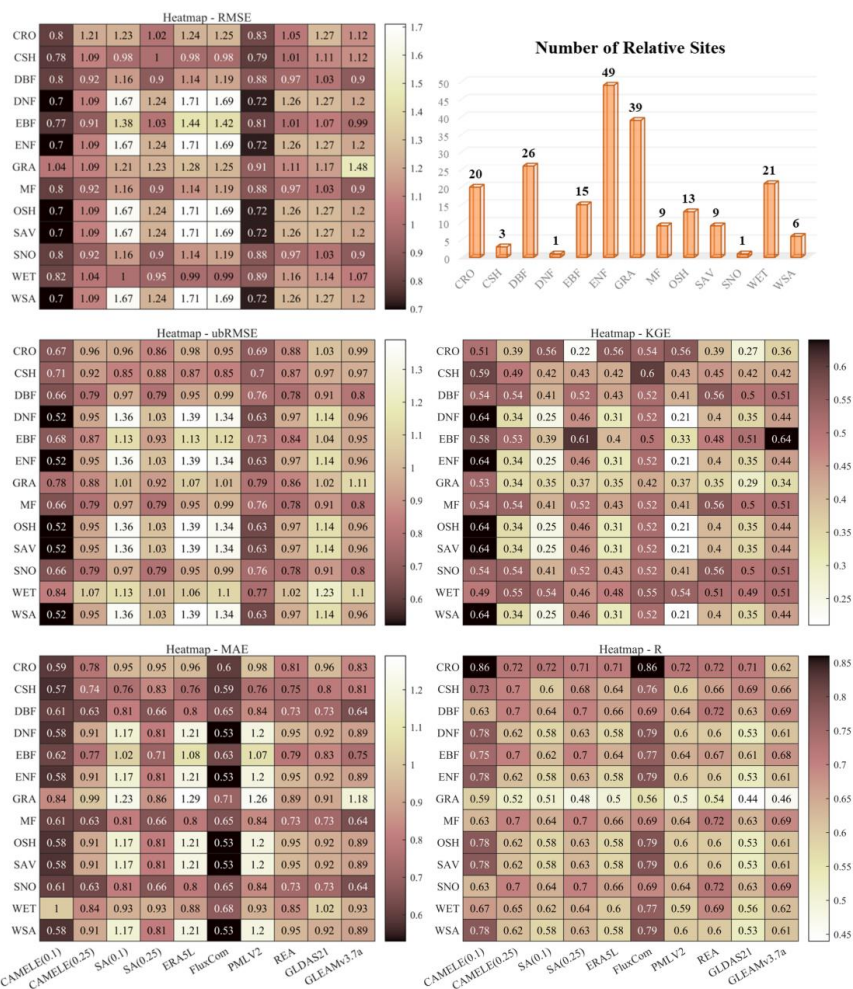


600 distribution, with the shaded area indicating the box plot, the dot representing the
 601 mean, and the right side showing the histogram.

602 **Table.4** Average values of indicators corresponding to different products, calculated
 603 based on the comprehensive results obtained for each site. The bolded sections
 604 indicate the schemes with the best performance in their respective metrics.

Product	RMSE (mm/d)	ubRMSE (mm/d)	MAE (mm/d)	KGE	R	
0.1°-daily	CAMELE	0.83	0.71	0.64	0.54	0.71
	SA	1.05	0.93	0.82	0.43	0.61
	ERA5L	1.05	0.94	0.82	0.43	0.63
	FluxCom	1.07	0.93	0.64	0.53	0.74
	PMLv2	0.84	0.74	0.84	0.43	0.61
0.25°-daily	CAMELE	1.03	0.87	0.75	0.49	0.67
	SA	0.97	0.84	0.80	0.45	0.66
	REA	1.02	0.86	0.80	0.47	0.67
	GLDAS21	1.10	0.97	0.83	0.43	0.63
	GLEAMv3.7a	1.03	0.93	0.79	0.46	0.64

605 Table 4 presents the average values of different metrics in Figure 5, boldly
 606 highlighting the optimal products corresponding to each metric. It can be observed
 607 that CAMELE exhibits significant improvements in performance at a resolution of
 608 0.1°, particularly in terms of the error metrics RMSE and ubRMSE, surpassing other
 609 products. This further confirms the effectiveness of our fusion scheme in reducing
 610 product errors. Additionally, although the performance of CAMELE at a resolution of
 611 0.25° is comparable to other products, there is still a slight decline compared to its
 612 performance at 0.1°. This can be attributed partly to the inherent errors in the input
 613 products and partly to the decreasing representativeness of FluxNet, which serves as
 614 the reference at the 0.25° grid. Nevertheless, we can still consider CAMELE to have
 615 good accuracy.



616

617

618

619

620

Figure.6 Heatmap of five indicators calculated separately for each site, classified by PFTs. The top right corner indicates the number of sites corresponding to each type.

Table.5 Optimal product corresponding to different PFTs under various statistical indicators against observations from FluxNet sites

IGBP (n-sites)	RMSE (mm/d)	ubRMSE (mm/d)	MAE (mm/d)	KGE	R
<i>CRO</i> (20)	CAMELE	CAMELE	CAMELE	PMLv2	FluxCom
<i>CSH</i> (3)		PMLv2		FluxCom	
<i>DBF</i> (26)		CAMELE		REA	
<i>DNF</i> (1)		CAMELE		CAMELE	



<i>EBF</i> (15)			CAMELE	GLEAM		
<i>ENF</i> (49)			FluxCom	CAMELE		
<i>GRA</i> (39)	PMLv2				CAMELE	
<i>MF</i> (9)	CAMELE		CAMELE	REA	FluxCom	
<i>OSH</i> (13)			FluxCom	CAMELE		
<i>SAV</i> (9)						
<i>SNO</i> (1)			CAMELE	REA		
<i>WET</i> (21)		PMLv2		FluxCom		CAMELE
<i>WSA</i> (6)		CAMELE				

621 Furthermore, we classified 212 sites according to PFTs and analyzed the statistical
 622 indicators of different PFTs corresponding to each site. The results are represented in
 623 Figure 6 as a heatmap, and the corresponding optimal products for other PFTs sites
 624 are marked in Table 5. The results show that CAMELE performs the best in almost all
 625 PFTs categories, as indicated by various indicators. While on sites where other
 626 products perform better, CAMELE's indicators are comparable to the optimal
 627 products, albeit slightly inferior. This indicates that our fusion approach effectively
 628 combines the advantages of different products, resulting in superior fusion results
 629 across different vegetation types.

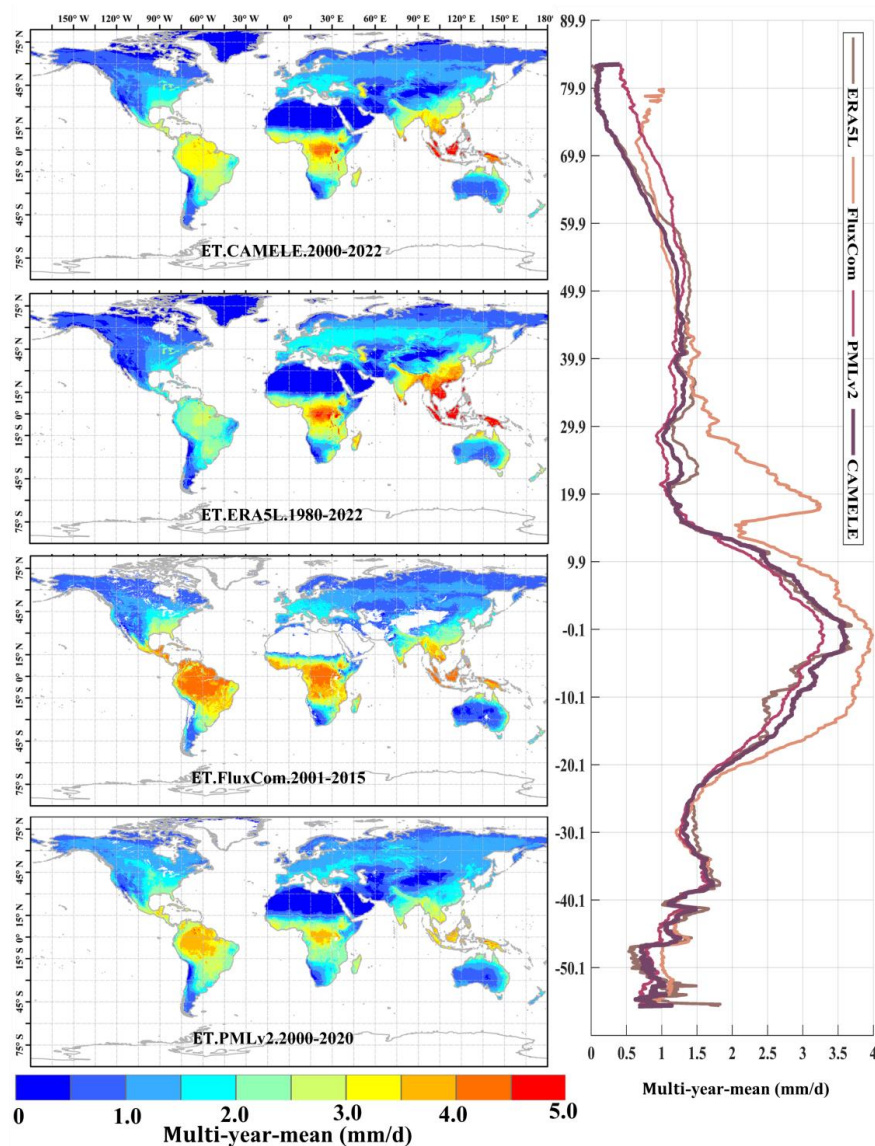
630 In summary, using the filtered daily-scale data from 212 FluxNet sites as a reference,
 631 we conducted a benchmark analysis with CAMELE and demonstrated its good fit
 632 with the observed data. Additionally, by comparing the performance of different
 633 products at each site, we further illustrated that CAMELE exhibits similar or slightly
 634 improved accuracy and minor errors compared to existing products.

635 4.3. Global comparison of multi-year average and linear trend

636 This section will compare the multi-year average daily-scale evapotranspiration
 637 distributions and their linear trends between CAMELE and other products at
 638 resolutions of 0.1° and 0.25°. Due to the varying available periods of different
 639 products, the results presented here are based on calculations using data from all



640 available periods, and the corresponding periods are indicated in each figure.

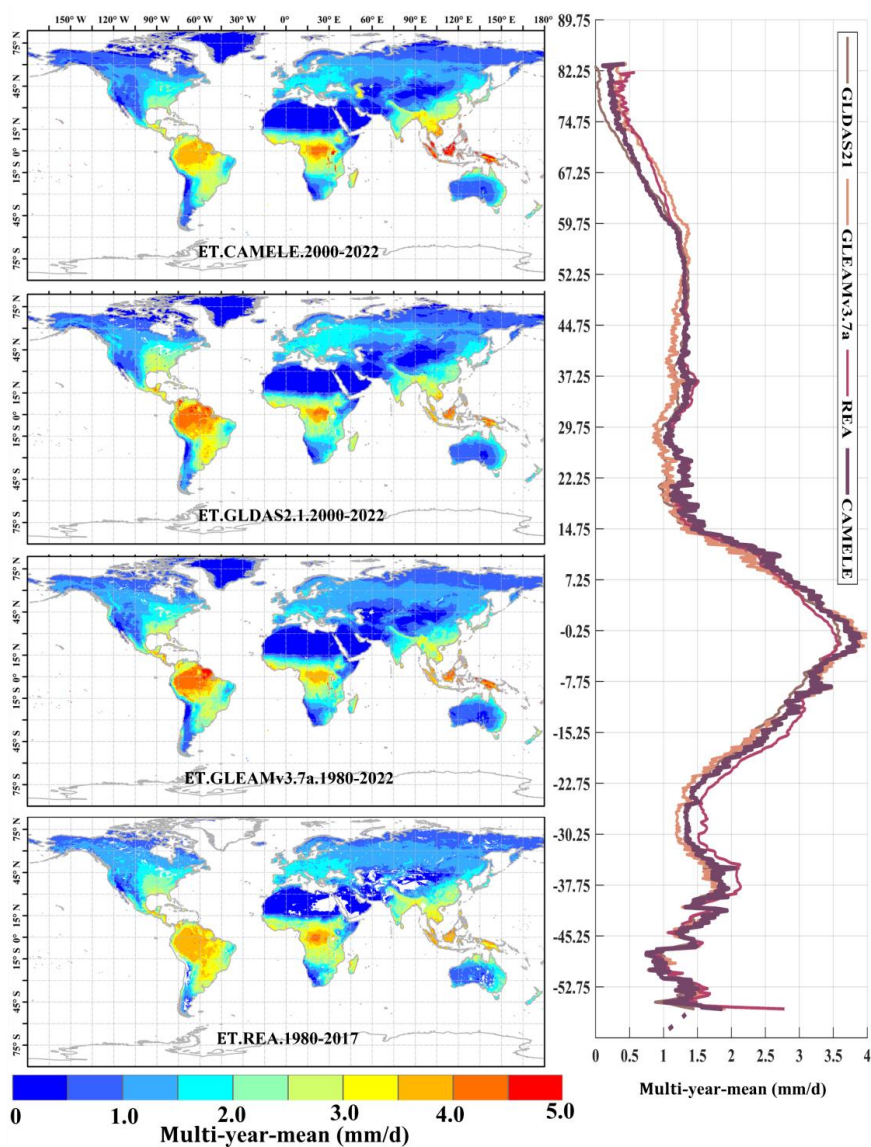


641
642 **FIGURE.7** Global distribution of multi-year daily average ET at 0.1° for CAMELE,
643 ERA5L, FluxCom, and PMLv2, depicted alongside corresponding variation curves of
644 average with latitude.
645 The results in Figure 7 indicate significant differences in the multi-year daily average
646 distribution of global evapotranspiration (ET) among different products. Specifically,

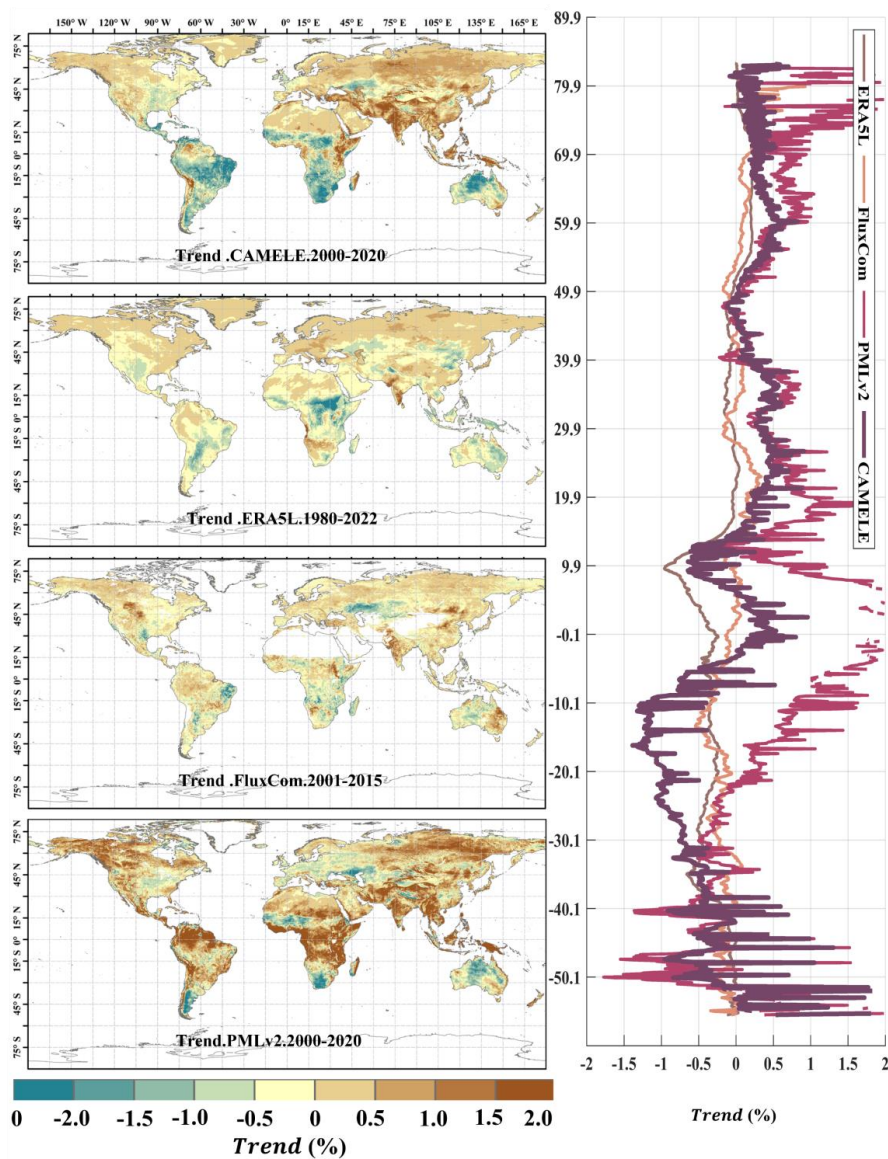


647 ERA5L shows noticeably higher values in East Asia than other products, while
648 FluxCom and PMLv2 exhibit higher values in the Amazon rainforest and southern
649 Africa regions. This distribution pattern is consistent with the error results obtained
650 from the EIVD calculation, indicating that these products possess certain uncertainties
651 in the regions. In terms of the latitudinal distribution pattern, except for FluxCom,
652 which displays distinct fluctuations, the variability among the other products is
653 relatively similar. This suggests that despite spatial differences among the different
654 products, they maintain consistency in the overall quantity.

655 Figure 8 presents the results with a resolution of 0.25° . It can be observed that
656 compared to the 0.1° distribution, the spatial distribution of annual average
657 evapotranspiration (ET) is more consistent among different products at 0.25° ,
658 showing larger ET values in tropical regions. The main differences are concentrated
659 in the Amazon rainforest and the Congo Basin, where GLEAM and GLDAS results
660 are higher than REA's. REA utilizes MERRA2 as input data, while GLDAS and
661 GLEAM have weights of approximately close to $1/3$ each (Lu et al., 2021). Therefore,
662 the distribution of REA falls between GLDAS and GLEAM, which is understandable.
663 The latitude variation plots show that the results from each product are very close,
664 providing additional evidence for the reliability of CAMELE.



665
666 **FIGURE.8** Global distribution of multi-year daily average ET at 0.25° for CAMELE,
667 GLDAS2.1, GLEAMv3.7a, and REA, depicted alongside corresponding variation
668 curves of average with latitude.



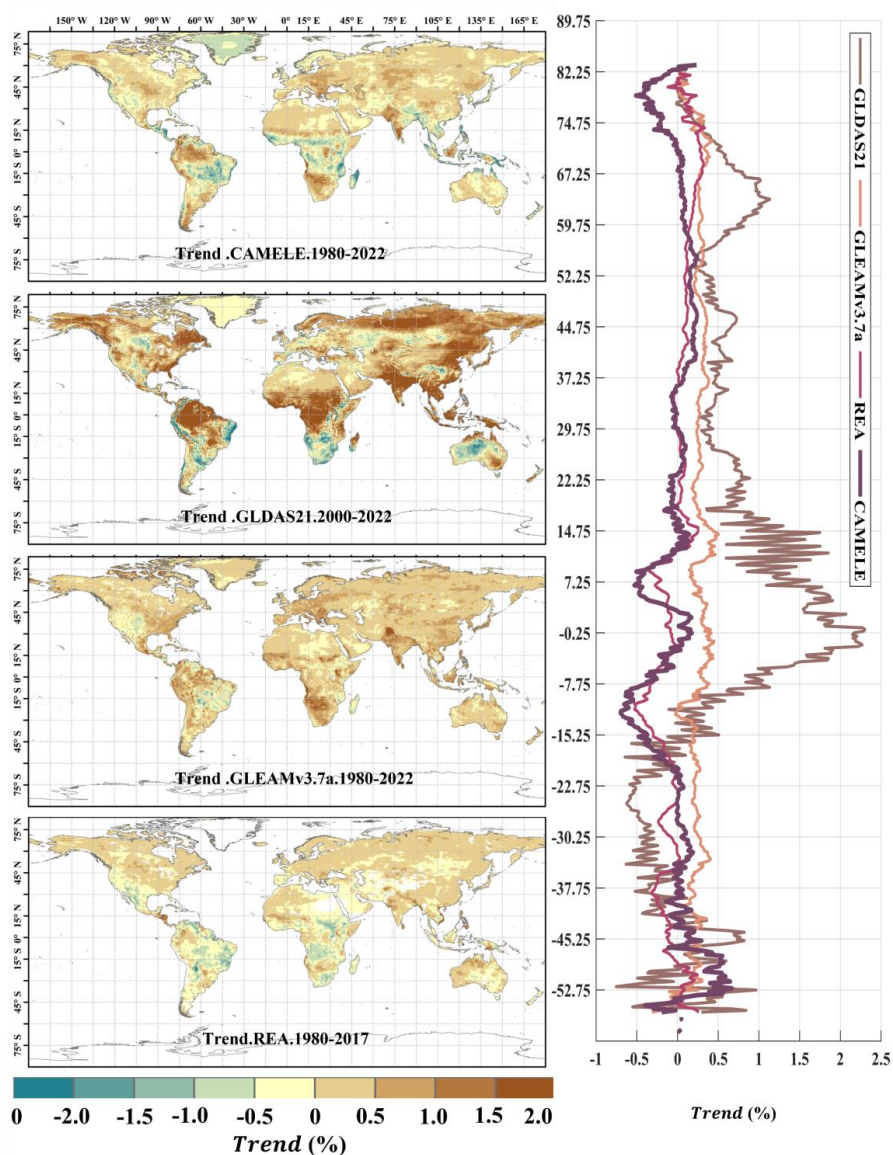
669

670

671

672

FIGURE.9 Global distribution of multi-year linear trend at 0.1° for CAMELE, ERA5L, FluxCom, and PMLv2, depicted alongside corresponding variation curves of average with latitude.



673

674 **FIGURE.10** Global distribution of multi-year linear trend at 0.25° for CAMELE,
675 GLDAS2.1, GLEAMv3.7a, and REA, depicted alongside corresponding variation
676 curves of average with latitude.

677 Figures 9 and 10 present the linear trends of multi-year daily scale evapotranspiration
678 (ET) calculated for different products at resolutions of 0.1° and 0.25°, respectively.
679 The corresponding latitude-dependent variations of the rate of change are shown on



680 the right side. It can be observed that the differences in linear trends among the
681 different products are more significant than the multi-year averages, and in some
682 regions, they even exhibit opposite trends. For example, at 0.1° resolution, PMLv2
683 shows a global increase of 1.0% in ET in most regions, while the results from
684 CAMELE, ERA5L, and PMLv2 indicate a slight decrease in ET in the Amazon
685 rainforest, southern Africa, and northwestern Australia. Among them, CAMELE
686 exhibits a more pronounced decreasing trend. At 0.25° resolution, except for
687 GLDAS2.1, which shows an apparent global increase in ET, the results from
688 CAMELE, GLEAMv3.7a, and REA indicate more minor variations in global ET.
689 To calculate the linear trend more reasonably, we focused on the available years for
690 different products without uniformly applying the same time range, as this could
691 introduce specific impacts on the comparison of results. Furthermore, it can be
692 observed that the linear trend obtained at 0.25° is milder than that of 0.1° . The grid
693 size and the characteristics of the data itself influence this.

694 **5. Discussion**

695 **5.1. Impact of underlying assumptions in collocation analysis**

696 The collocation analysis system relies on several fundamental assumptions, namely: (i)
697 Linearity: a linear regression model that describes the relationship between the true
698 signal and the datasets; (ii) Stationarity: the unconditional joint probability
699 distribution of the signal and the random error of estimates remains unchanged when
700 shifted in time; (iii) Error Orthogonality: independence between the random error of
701 estimates (e.g., evapotranspiration product) and the true signal (assumed unknown
702 true evapotranspiration value); and (iv) Zero Error Cross-Correlation: independence
703 between random errors of relevant datasets. Additionally, potential error
704 autocorrelation must be considered when incorporating the lag-1 [day] series into the
705 triplet (Kim et al., 2021b; Dong et al., 2020a, 2019). Numerous studies have



706 examined the validity of these assumptions and their impact on the outcomes if
707 violated (Tsamalis, 2022; Duan et al., 2021; Gruber et al., 2020). Thus, we will
708 provide a concise and accurate account of the implications resulting from breaches of
709 these assumptions.

710 The linearity assumption shapes the error model by including additive and
711 multiplicative biases and zero-mean random error. Although some studies have
712 explored the application of a nonlinear rescaling technique (Yilmaz and Crow, 2013;
713 Zwieback et al., 2016), those efforts are primarily limited to soil moisture signals and
714 often fail to accurately represent the true signal unless all datasets share a similar
715 signal-to-noise ratio (SNR). However, it is worth noting that after rescaling processes,
716 such as cumulative distribution function (CDF) matching or climatology removal, the
717 resulting time series (anomalies) are often considered linearly related to the truth since
718 higher-order error terms are removed. Therefore, the linear error model remains a
719 robust implementation, though it has the potential for improvement through rescaling
720 techniques.

721 Regarding violating the stationarity assumption, the evapotranspiration signal does
722 not strictly adhere to this characteristic. However, by collocating triplets with similar
723 magnitude variations, the influence of this violation is minimized. Nonetheless,
724 disparities in climatology between datasets can still arise for various reasons (Su and
725 Ryu, 2015). Several proposed alternatives aim to address this issue, such as removing
726 the climatology of inputs (Stoffelen, 1998; Yilmaz and Crow, 2014; Draper et al.,
727 2013) and subsequently analyzing the random error variance of the anomalies (Dong
728 et al., 2020b). Nevertheless, obtaining a reliable estimation of climatology proves
729 challenging in practice.

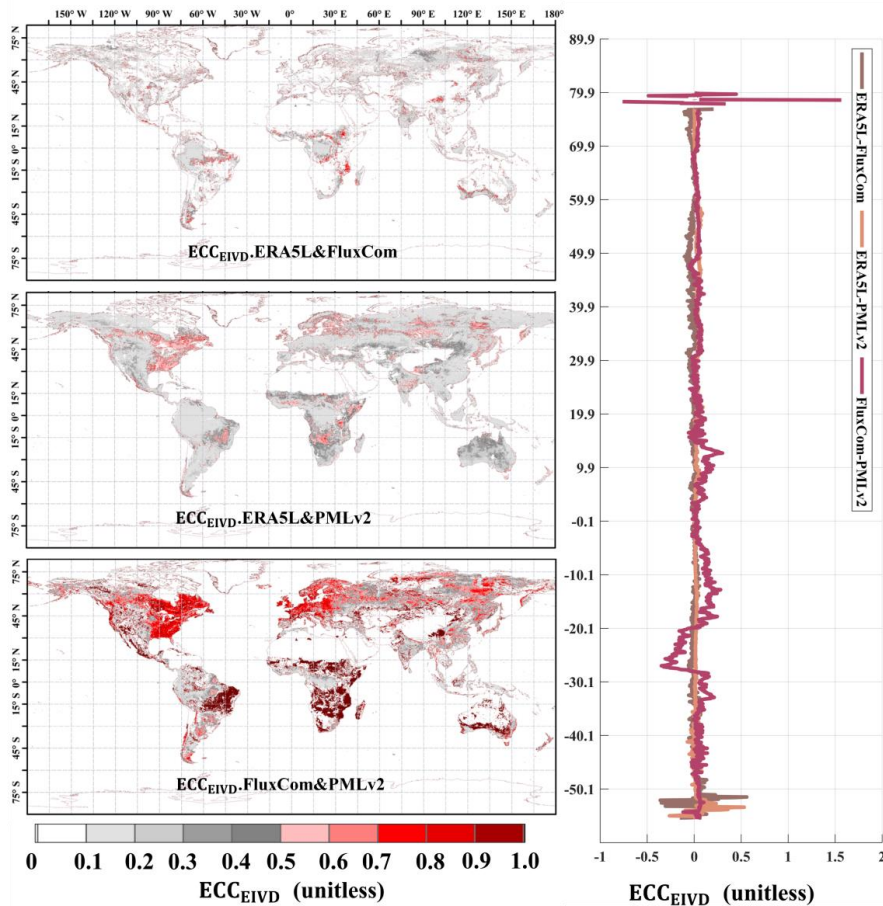
730 The assumption of error orthogonality assumes independence between random error
731 and true signal, i.e., $\sigma_{\varepsilon_t\theta} = 0$. A few studies have examined this assumption. Yilmaz
732 and Crow (2014) investigated such violations using four in situ sites and concluded
733 that the impact is negligible since rescaling mitigates or compensates for bias.



734 Additionally, non-orthogonality results in non-zero error cross-correlation (ECC),
735 although the latter is considered more important. Vogelzang et al. (2022) also
736 investigated this violation recently and demonstrated minimal second-order impact.
737 Non-zero ECC conditions introduce more substantial bias in the results compared to
738 other violations mainly due to two reasons: (1) they cannot be mitigated by rescaling;
739 (2) they cannot be compensated even with equal magnitude for all inputs; and (3) they
740 have been frequently reported in recent studies for various variables (Li et al., 2018,
741 2022; Gruber et al., 2016b). Gruber et al. (2016a) proposed the extended collocation
742 method, which effectively addresses the ECC of selected pairs. Moreover, the EIVD
743 method adopts the error cross-correlation framework. In the following section, we
744 will analyze the ECC between pairs.

745 **5.2. Analysis of error cross-correlation**

746 This study assumes non-zero ECC (Error-Correction Coefficient) conditions exist
747 between FluxCom and PMLv2 at 0.1° and between ERA5L and GLEAM at 0.25° .
748 However, non-zero ECC conditions were also possible between other pairs. Therefore,
749 we presented the EIVD-based ECC results of various pairs.



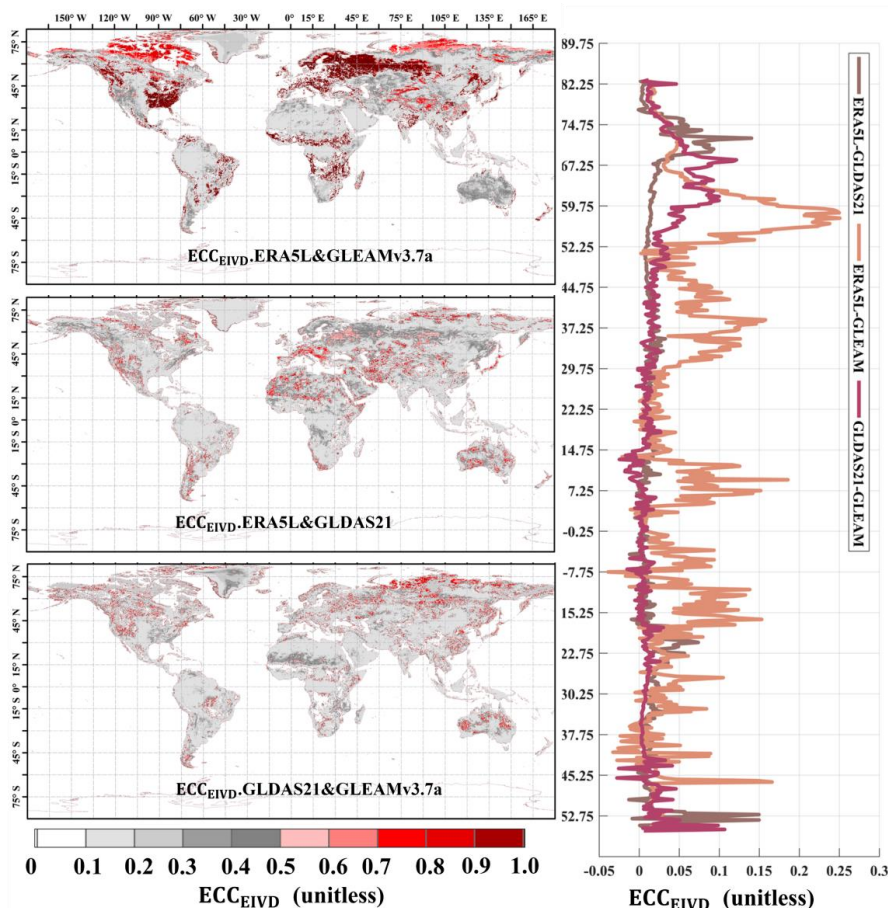
750

751 **FIGURE.11** Global Distribution of estimated error cross-correlation (ECC) between

752 ERA5L, FluxCom, and PMLv2 pairwise using EIVD alongside relevant variation

753 curves of average with latitude.

754



755

756 **FIGURE.12** Global Distribution of estimated error cross-correlation (ECC) between
757 ERA5L, GLEAMv3.7a, and GLDAS21 pairwise using EIVD alongside relevant
758 variation curves of average with latitude.

759 As depicted in Figure 11 and Figure 12, at a resolution of 0.1° , the Error-to-
760 Covariance (ECC) values of FluxCom and PMLv2 were notably higher than those of
761 ERA5L-FluxCom and ERA5L-PMLv2. The global average ECC value for FluxCom-
762 PMLv2 was 0.16, and regions with high ECC values were identified in the eastern
763 United States, most of Europe, and the western Amazon, areas densely covered by
764 measurement sites. Since both FluxCom and PMLv2 incorporated corrections based
765 on FluxNet measurement sites, there is likely some overlap between the sites by



766 both products in the high ECC regions. This partially explains the shared source of
767 random errors between the two datasets.

768 The global error correlations of GLEAM-GLDAS and ERA5L-GLDAS are relatively
769 low. The random error of ERA5L correlates with that of GLEAM, primarily in arid
770 regions such as the Sahara Desert, Northwest China, and central Australia, where the
771 average ECC exceeds 0.20. The global average ECC of ERA5L-GLEAM is
772 approximately 0.14. A higher error correlation is observed for ERA5L-GLEAM, with
773 a mean ECC value of 0.26, which is expected since meteorological information from
774 ECMWF is reanalyzed for both datasets. However, ECC values for GLEAM-GLDAS
775 and ERA5L-GLDAS are generally low globally, supporting the assumption of zero
776 ECC for these two pairs.

777 Our findings highlight the significant impact of Error Cross Correlation (ECC)
778 between FluxCom-PMLv2 and ERA5L-GLEAM at 0.1° and 0.25° resolutions,
779 respectively. Mathematically, when a triplet exhibits a high ECC value (>0.3)
780 between two sets, it indicates a preference for the remaining independent product as
781 the "better" one, potentially leading to an underestimation of its error variance.
782 However, it is essential to note that the overall ECC values for other pairs are
783 relatively small, suggesting that the zero ECC assumptions can be considered valid
784 for these pairs across most areas. Therefore, these assumptions are unlikely to affect
785 the relevant results of uncertainties significantly. Nevertheless, we have considered
786 the non-zero ECC condition between FluxCom-PMLv2 and ERA5L-GLEAM in this
787 study, as it requires careful consideration.

788 **5.3. Comparison of different fusion schemes**

789 In this section, we conducted comparisons in three aspects: (1) comparing the
790 performance of CAMELE at different resolutions; (2) comparing the performance of
791 different change fusion schemes, explicitly changing the input products' versions
792 (GLDAS21 to GLDAS22, GLEAMv3.7a to v3.7b); and (3) comparing the



793 performance of the results obtained without considering the ECC impact.
794 We compared the results of three schemes in the fusion process at a resolution of
795 0.25° . The first combination consisted of ERA5L, GLDAS22, and GLEAMv3.7a
796 (Comb1). The second input combination consisted of ERA5L, GLDAS22, and
797 GLEAMv3.7b (Comb2). The third input combination consisted of ERA5L,
798 GLDAS2.1, and GLEAMv3.7b (denoted as Comb3). These three combinations used
799 for comparison corresponded to the period from February 2003 to December 2022.
800 The combination assuming zero ECC (Zero-ECC) had the same inputs as CAMELE
801 at both resolutions.

802 **Table 6** Average metrics for CAMELE and other fusion schemes at all sites. The
803 bolded sections indicate the schemes with the best performance in their respective
804 metrics.

Product	RMSE (mm/d)	ubRMSE (mm/d)	MAE (mm/d)	KGE	R
CAMELE (0.1)	0.83	0.71	0.64	0.54	0.71
CAMELE (0.25)	1.03	0.87	0.75	0.49	0.67
Comb1	1.20	0.95	0.94	0.43	0.68
Comb2	1.19	0.94	0.93	0.44	0.69
Comb3	1.05	0.90	0.80	0.47	0.69
Zero-ECC (0.1)	1.06	0.91	0.80	0.44	0.60
Zero-ECC (0.25)	1.26	1.03	0.99	0.38	0.61

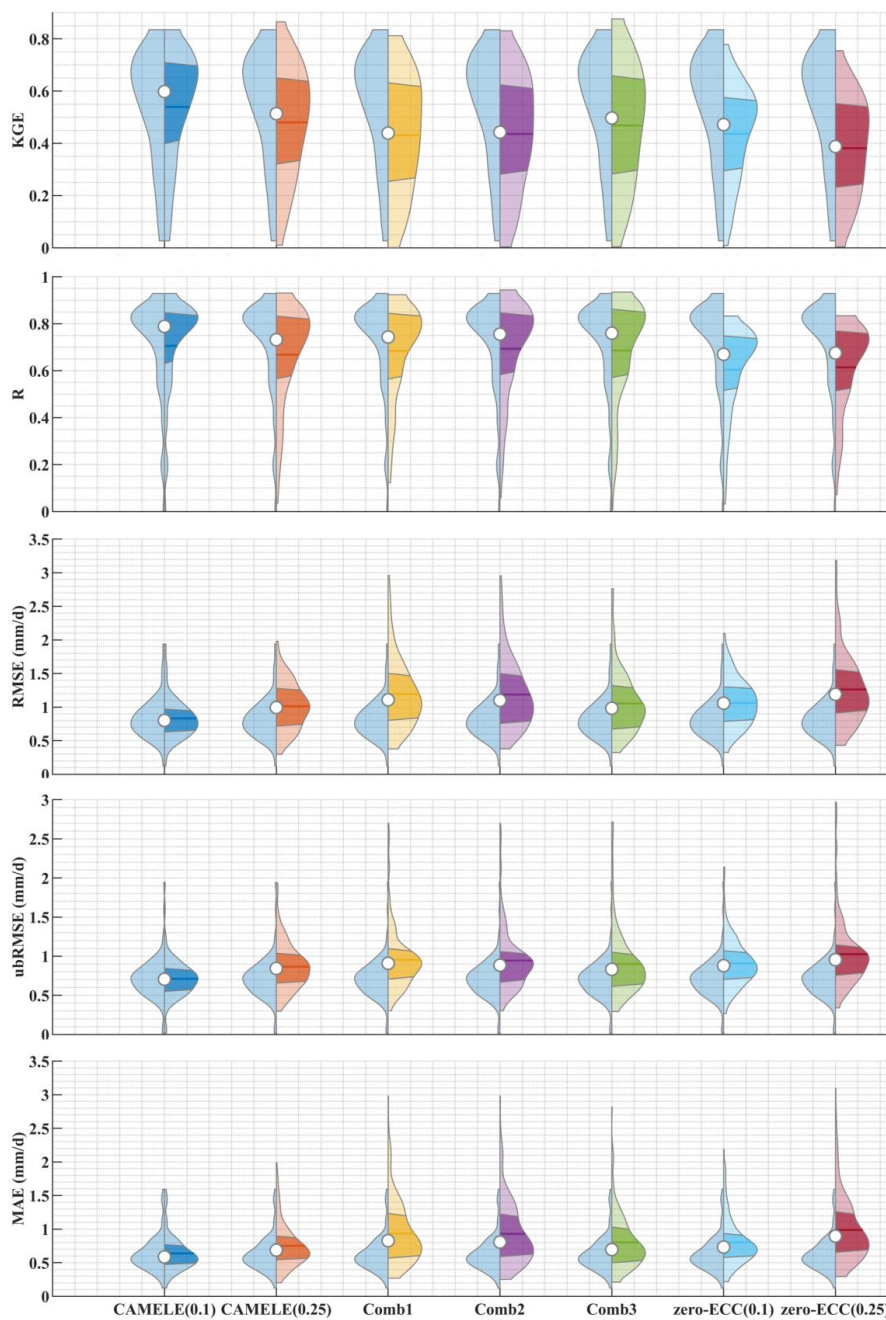
805 According to the information in the table, CAMELE (0.1°) results were superior in all
806 indicators. Firstly, when comparing the performance of CAMELE at resolutions of
807 0.1° and 0.25° , it was observed that the fused product performed slightly worse at the
808 0.25° resolution. This could be attributed to the variations in the input products.
809 Additionally, the representative of FluxNet sites at the 0.25° resolution decreased,
810 leading to degraded statistical indicators.

811 Furthermore, when comparing the results of different fusion schemes, mainly
812 focusing on the differences between CAMELE and Comb1 to Comb3 at the 0.25°
813 resolution, CAMELE performed better regarding error metrics (RMSE, ubRMSE,



814 MAE). The differences in fitting metrics (KGE, R) were insignificant, indicating that
815 the choice of fusion scheme primarily affected the errors of the fusion results. The
816 relatively poor performance of other fusion schemes could be due to the lack of
817 consideration for non-zero ECC. For example, GLEAMv3.7b and GLDAS2.2
818 employed the satellite data from MODIS, introducing random error homogeneity
819 between the two datasets.

820 Moreover, when comparing the fusion effects with and without considering non-zero
821 ECC conditions, it was evident that considering ECC information could effectively
822 improve the performance of the fused product, which further demonstrated the
823 reliability and advantages of the fusion method employed in this study.



824

825 **Figure 13** Violin plot comparing KGE, R, RMSE, ubRMSE and MAE of CAMELE
826 with other fusion schemes. The right half of each violin plot represents the



827 distribution, with shaded areas indicating the box plot, where the horizontal line
828 corresponds to the median and the dot represents the mean. The left half represents
829 the results of CAMELE (0.1°) for comparison.

830 We further provided violin plots for different metrics, comparing the results of each
831 fusion scheme to CAMELE (0.1°). The results indicated that the fusion schemes
832 adopted were significantly superior to other schemes based on the distribution of
833 results for all metrics across all sites. Regarding KGE and R, CAMELE's results were
834 concentrated near 1 for most sites. Regarding RMSE, ubRMSE, and MAE, their
835 results were concentrated below one mm/d. The results in the plots also suggested that
836 CAMELE performed slightly worse at 0.25° compared to 0.1° but still outperformed
837 the combination results of Comb1 to Comb3. Additionally, comparing CAMELE and
838 the zero-ECC scheme in the plots further highlighted the importance of considering
839 non-zero ECC conditions.

840 **6. Conclusion**

841 This study used a collocation-based approach for merging data considering non-zero
842 conditions. We successfully generated a long-term daily CAMELE evapotranspiration
843 (ET) product at resolutions of 0.1° (2000 to 2020) and 0.25° (1980 to 2022) by
844 integrating five widely used datasets: ERA5L, FluxCom, PMLv2, GLDAS, and
845 GLEAM. The key findings of our study are as follows:

- 846 1. Collocation analysis methods proved to be a reliable tool for evaluating ET
847 products without a reference dataset. This approach shows promising potential for
848 error characterization, especially in regions with limited data availability or on a
849 global scale. The evaluation results provided valuable insights into the data
850 merging process.
- 851 2. Compared to five input products, REA, and simple average, the CAMELE product
852 performed well when evaluated against FluxNet flux tower data. Although it may
853 not have been the best in all metrics, the overall performance was satisfactory.



854 The result showed Pearson correlation coefficients (R) of 0.63 and 0.65, root-
855 mean-square errors (RMSE) of 0.81 and 0.73 mm/d, unbiased root-mean-square
856 errors (ubRMSE) of 1.20 and 1.04 mm/d, mean absolute errors (MAE) of 0.81 and
857 0.73 mm/d, and Kling-Gupta efficiency (KGE) of 0.60 and 0.65 on average over
858 resolutions of 0.1° and 0.25° , respectively.

859 3. For different plant functional types (PFTs), the CAMELE product outperformed
860 the five input products, REA, and simple average in most PFTs. Although
861 FluxCom and PMLv2 performed slightly better than CAMELE at some PFT sites,
862 considering that both utilized FluxNet sites for product calibration, it indirectly
863 demonstrates the excellent performance of CAMELE.

864 4. When utilizing the error information derived from collocation analysis for
865 merging, it is crucial to consider the potential presence of non-zero error
866 compensation conditions (ECC). Comparing the merging schemes with and
867 without considering non-zero ECC, it was found that considering ECC improves
868 the accuracy of the merging process. Additionally, when using collocation
869 analysis, it is necessary to identify which products may have ECC in advance,
870 providing more effective support for data merging and obtaining more accurate
871 product error information.

872 In conclusion, our proposed collocation-based data merging approach demonstrates
873 the promising potential for merging ET products. The resulting CAMELE product
874 exhibited good overall performance at site-based and regional scales, meeting the
875 requirements for more detailed research. Furthermore, further evaluation of the
876 merged product in specific regions is necessary to improve its accuracy. In future
877 studies, dynamic weights could be computed by considering suitable merging periods
878 for different products to enhance the quality of the merged product, and more
879 sophisticated combination schemes could be explored to improve accuracy.



880 **Author Contribution**

881 C.L. conceived and designed the study, collected and analyzed the data, and wrote the
882 manuscript. H.Y participated in the study design, provided intellectual insights, and
883 reviewed the manuscript for important intellectual content. Z.L. and W.Y provided
884 substantial input in the study design and data interpretation and revised the manuscript.
885 Z.T., J.H., and S.L. guided the research process and critically reviewed the manuscript.
886 All authors have read and approved the final version of the manuscript.

887 **Competing interests**

888 The authors declare that they have no conflict of interest.

889 **Acknowledgments**

890 This research was supported by the China National Key R&D Program (grant no.
891 2022YFC3002802), the National Natural Science Foundation of China (grant nos.
892 51979140, 42041004), and the Key Research and Development Program of Yunnan
893 Province, China (grant no. 202203AA080010).

894 **Data and code availability**

895 The datasets utilized in this research can be accessed through the links provided in the
896 Dataset Section. The CAMELE products are available via
897 <https://doi.org/10.5281/zenodo.5704736> (Li et al., 2023a). The data is distributed
898 under a Creative Commons Attribution 4.0 License. Additionally, we provide
899 example MATLAB codes to read and plot CAMELE data and employ IVD and EIVD
900 methods to merge the inputs. Please refer to the latest version., 202306.



901 Reference

- 902 Baker, J. C. A., Garcia-Carreras, L., Gloor, M., Marsham, J. H., Buermann, W., da
903 Rocha, H. R., Nobre, A. D., de Araujo, A. C., and Spracklen, D. V.:
904 Evapotranspiration in the Amazon: spatial patterns, seasonality, and recent trends in
905 observations, reanalysis, and climate models, *Hydrology and Earth System Sciences*,
906 25, 2279–2300, <https://doi.org/10.5194/hess-25-2279-2021>, 2021.
- 907 Barraza Bernadas, V., Grings, F., Restrepo-Coupe, N., and Huete, A.: Comparison of
908 the performance of latent heat flux products over southern hemisphere forest
909 ecosystems: estimating latent heat flux error structure using in situ measurements and
910 the triple collocation method, *International Journal of Remote Sensing*, 39, 6300–
911 6315, 2018.
- 912 Bates, J. M. and Granger, C. W.: The combination of forecasts, *Journal of the*
913 *Operational Research Society*, 20, 451–468, 1969.
- 914 Chen, Z., Zhu, Z., Jiang, H., and Sun, S.: Estimating daily reference
915 evapotranspiration based on limited meteorological data using deep learning and
916 classical machine learning methods, *Journal of Hydrology*, 591,
917 <https://doi.org/10.1016/j.jhydrol.2020.125286>, 2020.
- 918 De Lannoy, G. J., Houser, P. R., Verhoest, N. E., Pauwels, V. R., and Gish, T. J.:
919 Upscaling of point soil moisture measurements to field averages at the OPE3 test site,
920 *Journal of Hydrology*, 343, 1–11, 2007.
- 921 Deng, X., Zhu, L., Wang, H., Zhang, X., Tong, C., Li, S., and Wang, K.: Triple
922 Collocation Analysis and In Situ Validation of the CYGNSS Soil Moisture Product,
923 *IEEE Journal of Selected Topics in Applied Earth Observations and Remote Sensing*,
924 16, 1883–1899, <https://doi.org/10.1109/jstars.2023.3235111>, 2023.
- 925 Dong, J. and Crow, W. T.: An Improved Triple Collocation Analysis Algorithm for
926 Decomposing Autocorrelated and White Soil Moisture Retrieval Errors, *Journal of*
927 *Geophysical Research: Atmospheres*, 122, 13,081–13,094,
928 <https://doi.org/10.1002/2017jd027387>, 2017.
- 929 Dong, J., Crow, W. T., Duan, Z., Wei, L., and Lu, Y.: A double instrumental variable
930 method for geophysical product error estimation, *Remote Sensing of Environment*,
931 225, 217–228, <https://doi.org/10.1016/j.rse.2019.03.003>, 2019.
- 932 Dong, J., Wei, L., Chen, X., Duan, Z., and Lu, Y.: An instrument variable based
933 algorithm for estimating cross-correlated hydrological remote sensing errors, *Journal*
934 *of Hydrology*, 581, 124413, <https://doi.org/10.1016/j.jhydrol.2019.124413>, 2020a.
- 935 Dong, J., Lei, F., and Wei, L.: Triple Collocation Based Multi-Source Precipitation
936 Merging, *Frontiers in Water*, 2, <https://doi.org/10.3389/frwa.2020.00001>, 2020b.
- 937 Dong, J., Crow, W. T., Chen, X., Tangdamrongsub, N., Gao, M., Sun, S., Qiu, J., Wei,
938 L., Gao, H., and Duan, Z.: Statistical uncertainty analysis-based precipitation merging
939 (SUPER): A new framework for improved global precipitation estimation, *Remote*
940 *Sensing of Environment*, 283, 113299, <https://doi.org/10.1016/j.rse.2022.113299>,



- 941 2022.
- 942 Dorigo, W. A., Scipal, K., Parinussa, R. M., Liu, Y. Y., Wagner, W., De Jeu, R. A.,
943 and Naeimi, V.: Error characterisation of global active and passive microwave soil
944 moisture datasets, *Hydrology and Earth System Sciences*, 14, 2605–2616, 2010.
- 945 Draper, C., Reichle, R., de Jeu, R., Naeimi, V., Parinussa, R., and Wagner, W.:
946 Estimating root mean square errors in remotely sensed soil moisture over continental
947 scale domains, *Remote Sensing of Environment*, 137, 288–298, 2013.
- 948 Duan, Z., Duggan, E., Chen, C., Gao, H., Dong, J., and Liu, J.: Comparison of
949 traditional method and triple collocation analysis for evaluation of multiple gridded
950 precipitation products across Germany, *Journal of Hydrometeorology*,
951 <https://doi.org/10.1175/JHM-D-21-0049.1>, 2021.
- 952 ECMWF, S. P.: In IFS documentation CY40R1 Part IV: Physical Processes, ECMWF:
953 Reading, UK, 111–113, 2014.
- 954 Ershadi, A., McCabe, M. F., Evans, J. P., Chaney, N. W., and Wood, E. F.: Multi-site
955 evaluation of terrestrial evaporation models using FLUXNET data, *Agricultural and
956 Forest Meteorology*, 187, 46–61, <https://doi.org/10.1016/j.agrformet.2013.11.008>,
957 2014.
- 958 Feng, Y., Cui, N., Zhao, L., Hu, X., and Gong, D.: Comparison of ELM, GANN,
959 WNN and empirical models for estimating reference evapotranspiration in humid
960 region of Southwest China, *Journal of Hydrology*, 536, 376–383,
961 <https://doi.org/10.1016/j.jhydrol.2016.02.053>, 2016.
- 962 Gan, R., Zhang, Y., Shi, H., Yang, Y., Eamus, D., Cheng, L., Chiew, F. H., and Yu,
963 Q.: Use of satellite leaf area index estimating evapotranspiration and gross
964 assimilation for Australian ecosystems, *Ecohydrology*, 11, e1974, 2018.
- 965 Gentine, P., Massmann, A., Lintner, B. R., Hamed Alemohammad, S., Fu, R., Green,
966 J. K., Kennedy, D., and Vilà-Guerau de Arellano, J.: Land–atmosphere interactions in
967 the tropics – a review, *Hydrology and Earth System Sciences*, 23, 4171–4197,
968 <https://doi.org/10.5194/hess-23-4171-2019>, 2019.
- 969 Gruber, A.: Estimation of error structures in remotely sensed soil moisture data sets,
970 Wien, 2016.
- 971 Gruber, A., Su, C., Crow, W. T., Zwieback, S., Dorigo, W., and Wagner, W.:
972 Estimating error cross-correlations in soil moisture data sets using extended
973 collocation analysis, *Journal of Geophysical Research: Atmospheres*, 121, 1208–1219,
974 2016a.
- 975 Gruber, A., Su, C.-H., Zwieback, S., Crow, W., Dorigo, W., and Wagner, W.: Recent
976 advances in (soil moisture) triple collocation analysis, *International Journal of
977 Applied Earth Observation and Geoinformation*, 45, 200–211,
978 <https://doi.org/10.1016/j.jag.2015.09.002>, 2016b.
- 979 Gruber, A., Dorigo, W. A., Crow, W., and Wagner, W.: Triple Collocation-Based
980 Merging of Satellite Soil Moisture Retrievals, *IEEE Trans. Geosci. Remote Sensing*,
981 55, 6780–6792, <https://doi.org/10.1109/TGRS.2017.2734070>, 2017.
- 982 Gruber, A., Scanlon, T., van der Schalie, R., Wagner, W., and Dorigo, W.: Evolution



- 983 of the ESA CCI Soil Moisture climate data records and their underlying merging
984 methodology, *Earth System Science Data*, 11, 717–739, [https://doi.org/10.5194/essd-](https://doi.org/10.5194/essd-11-717-2019)
985 11-717-2019, 2019.
- 986 Gruber, A., De Lannoy, G., Albergel, C., Al-Yaari, A., Brocca, L., Calvet, J. C.,
987 Colliander, A., Cosh, M., Crow, W., Dorigo, W., Draper, C., Hirschi, M., Kerr, Y.,
988 Konings, A., Lahoz, W., McColl, K., Montzka, C., Muñoz-Sabater, J., Peng, J.,
989 Reichle, R., Richaume, P., Rüdiger, C., Scanlon, T., van der Schalie, R., Wigneron, J.
990 P., and Wagner, W.: Validation practices for satellite soil moisture retrievals: What
991 are (the) errors?, *Remote Sensing of Environment*, 244, 111806,
992 <https://doi.org/10.1016/j.rse.2020.111806>, 2020.
- 993 Gupta, H. V., Kling, H., Yilmaz, K. K., and Martinez, G. F.: Decomposition of the
994 mean squared error and NSE performance criteria: Implications for improving
995 hydrological modelling, *Journal of hydrology*, 377, 80–91, 2009.
- 996 Han, S. and Tian, F.: A review of the complementary principle of evaporation: from
997 the original linear relationship to generalized nonlinear functions, *Hydrology and*
998 *Earth System Sciences*, 24, 2269–2285, <https://doi.org/10.5194/hess-24-2269-2020>,
999 2020.
- 1000 Hao, Y., Baik, J., and Choi, M.: Combining generalized complementary relationship
1001 models with the Bayesian Model Averaging method to estimate actual
1002 evapotranspiration over China, *Agricultural and Forest Meteorology*, 279, 107759,
1003 <https://doi.org/10.1016/j.agrformet.2019.107759>, 2019.
- 1004 Hersbach, H., Bell, B., Berrisford, P., Hirahara, S., Horányi, A., Muñoz-Sabater, J.,
1005 Nicolas, J., Peubey, C., Radu, R., Schepers, D., Simmons, A., Soci, C., Abdalla, S.,
1006 Abellan, X., Balsamo, G., Bechtold, P., Biavati, G., Bidlot, J., Bonavita, M., Chiara,
1007 G., Dahlgren, P., Dee, D., Diamantakis, M., Dragani, R., Flemming, J., Forbes, R.,
1008 Fuentes, M., Geer, A., Haimberger, L., Healy, S., Hogan, R. J., Hólm, E., Janisková,
1009 M., Keeley, S., Laloyaux, P., Lopez, P., Lupu, C., Radnoti, G., Rosnay, P., Rozum, I.,
1010 Vamborg, F., Villaume, S., and Thépaut, J.: The ERA5 global reanalysis, *Quarterly*
1011 *Journal of the Royal Meteorological Society*, 146, 1999–2049,
1012 <https://doi.org/10.1002/qj.3803>, 2020.
- 1013 Hoareau, N., Portabella, M., Lin, W., Ballabrera-Poy, J., and Turiel, A.: Error
1014 characterization of sea surface salinity products using triple collocation analysis,
1015 *IEEE Transactions on Geoscience and Remote Sensing*, 56, 5160–5168, 2018.
- 1016 Jia, Y., Li, C., Yang, H., Yang, W., and Liu, Z.: Assessments of three
1017 evapotranspiration products over China using extended triple collocation and water
1018 balance methods, *Journal of Hydrology*, 614, 128594, 2022.
- 1019 Jiang, C. and Ryu, Y.: Multi-scale evaluation of global gross primary productivity and
1020 evapotranspiration products derived from Breathing Earth System Simulator (BESS),
1021 *Remote Sensing of Environment*, 186, 528–547, 2016.
- 1022 Jiang, C., Ryu, Y., Fang, H., Myneni, R., Claverie, M., and Zhu, Z.: Inconsistencies of
1023 interannual variability and trends in long-term satellite leaf area index products, *Glob*
1024 *Chang Biol*, 23, 4133–4146, <https://doi.org/10.1111/gcb.13787>, 2017.



- 1025 Jiang, C., Guan, K., Pan, M., Ryu, Y., Peng, B., and Wang, S.: BESS-STAIR: a
1026 framework to estimate daily, 30 m, and all-weather crop evapotranspiration using
1027 multi-source satellite data for the US Corn Belt, *Hydrology and Earth System*
1028 *Sciences*, 24, 1251–1273, <https://doi.org/10.5194/hess-24-1251-2020>, 2020.
- 1029 Jung, M., Koirala, S., Weber, U., Ichii, K., Gans, F., Camps-Valls, G., Papale, D.,
1030 Schwalm, C., Tramontana, G., and Reichstein, M.: The FLUXCOM ensemble of
1031 global land-atmosphere energy fluxes, *Sci Data*, 6, 74,
1032 <https://doi.org/10.1038/s41597-019-0076-8>, 2019.
- 1033 Khan, M. S., Liaqat, U. W., Baik, J., and Choi, M.: Stand-alone uncertainty
1034 characterization of GLEAM, GLDAS and MOD16 evapotranspiration products using
1035 an extended triple collocation approach, *Agricultural and Forest Meteorology*, 252,
1036 256–268, <https://doi.org/10.1016/j.agrformet.2018.01.022>, 2018.
- 1037 Kim, S., Pham, H. T., Liu, Y. Y., Marshall, L., and Sharma, A.: Improving the
1038 Combination of Satellite Soil Moisture Data Sets by Considering Error Cross
1039 Correlation: A Comparison Between Triple Collocation (TC) and Extended Double
1040 Instrumental Variable (EIVD) Alternatives, *IEEE Transactions on Geoscience and*
1041 *Remote Sensing*, 59, 7285–7295, <https://doi.org/10.1109/tgrs.2020.3032418>, 2021a.
- 1042 Kim, S., Sharma, A., Liu, Y. Y., and Young, S. I.: Rethinking satellite data merging:
1043 from averaging to SNR optimization, *IEEE Transactions on Geoscience and Remote*
1044 *Sensing*, 60, 1–15, 2021b.
- 1045 Knoben, W. J. M., Freer, J. E., and Woods, R. A.: Technical note: Inherent
1046 benchmark or not? Comparing Nash–Sutcliffe and Kling–Gupta efficiency scores,
1047 *Hydrology and Earth System Sciences*, 23, 4323–4331, [https://doi.org/10.5194/hess-](https://doi.org/10.5194/hess-23-4323-2019)
1048 [23-4323-2019](https://doi.org/10.5194/hess-23-4323-2019), 2019.
- 1049 Koster, R. D., Liu, Q., Reichle, R. H., and Huffman, G. J.: Improved Estimates of
1050 Pentad Precipitation Through the Merging of Independent Precipitation Data Sets,
1051 *Water Resources Research*, 57, <https://doi.org/10.1029/2021wr030330>, 2021.
- 1052 Leuning, R., Zhang, Y., Rajaud, A., Cleugh, H., and Tu, K.: A simple surface
1053 conductance model to estimate regional evaporation using MODIS leaf area index and
1054 the Penman-Monteith equation, *Water Resources Research*, 44, 2008.
- 1055 Leuning, R., Zhang, Y. Q., Rajaud, A., Cleugh, H., and Tu, K.: Correction to “A
1056 simple surface conductance model to estimate regional evaporation using MODIS leaf
1057 area index and the Penman-Monteith equation,” *Water Resources Research*, 45,
1058 <https://doi.org/10.1029/2008wr007631>, 2009.
- 1059 Li, B., Rodell, M., Kumar, S., Beaudoin, H. K., Getirana, A., Zaitchik, B. F.,
1060 Goncalves, L. G., Cossetin, C., Bhanja, S., Mukherjee, A., Tian, S., Tangdamrongsub,
1061 N., Long, D., Nanteza, J., Lee, J., Policelli, F., Goni, I. B., Daira, D., Bila, M., Lannoy,
1062 G., Mocko, D., Steele-Dunne, S. C., Save, H., and Bettadpur, S.: Global GRACE Data
1063 Assimilation for Groundwater and Drought Monitoring: Advances and Challenges,
1064 *Water Resour. Res.*, 55, 7564–7586, <https://doi.org/10.1029/2018WR024618>, 2019a.
- 1065 Li, C., Tang, G., and Hong, Y.: Cross-evaluation of ground-based, multi-satellite and
1066 reanalysis precipitation products: Applicability of the Triple Collocation method



- 1067 across Mainland China, *Journal of Hydrology*, 562, 71–83,
1068 <https://doi.org/10.1016/j.jhydrol.2018.04.039>, 2018.
- 1069 Li, C., Yang, H., Yang, W., Liu, Z., Jia, Y., Li, S., and Yang, D.: Error
1070 Characterization of Global Land Evapotranspiration Products: Collocation-based
1071 approach, *Journal of Hydrology*, 128102, 2022.
- 1072 Li, C., Liu, Z., Yang, W., Tu, Z., Han, J., Sien, L., and Hanbo, Y.: CAMELE:
1073 Collocation-Analyzed Multi-source Ensembled Land Evapotranspiration Data, ,
1074 <https://doi.org/10.5281/zenodo.8047038>, 2023a.
- 1075 Li, X., Gentine, P., Lin, C., Zhou, S., Sun, Z., Zheng, Y., Liu, J., and Zheng, C.: A
1076 simple and objective method to partition evapotranspiration into transpiration and
1077 evaporation at eddy-covariance sites, *Agricultural and Forest Meteorology*, 265, 171–
1078 182, <https://doi.org/10.1016/j.agrformet.2018.11.017>, 2019b.
- 1079 Li, X., Zhang, W., Vermeulen, A., Dong, J., and Duan, Z.: Triple collocation-based
1080 merging of multi-source gridded evapotranspiration data in the Nordic Region,
1081 *Agricultural and Forest Meteorology*, 335, 109451,
1082 <https://doi.org/10.1016/j.agrformet.2023.109451>, 2023b.
- 1083 Lian, X., Piao, S., Huntingford, C., Li, Y., Zeng, Z., Wang, X., Ciais, P., McVicar, T.
1084 R., Peng, S., Ottlé, C., Yang, H., Yang, Y., Zhang, Y., and Wang, T.: Partitioning
1085 global land evapotranspiration using CMIP5 models constrained by observations,
1086 *Nature Clim Change*, 8, 640–646, <https://doi.org/10.1038/s41558-018-0207-9>, 2018.
- 1087 Liang, S., Cheng, J., Jia, K., Jiang, B., Liu, Q., Xiao, Z., Yao, Y., Yuan, W., Zhang,
1088 X., Zhao, X., and Zhou, J.: The Global Land Surface Satellite (GLASS) Product Suite,
1089 *Bulletin of the American Meteorological Society*, 102, E323–E337,
1090 <https://doi.org/10.1175/bams-d-18-0341.1>, 2021.
- 1091 Lin, C., Gentine, P., Huang, Y., Guan, K., Kimm, H., and Zhou, S.: Diel ecosystem
1092 conductance response to vapor pressure deficit is suboptimal and independent of soil
1093 moisture, *Agricultural and Forest Meteorology*, 250, 24–34, 2018.
- 1094 Loveland, T. R., Zhu, Z., Ohlen, D. O., Brown, J. F., Reed, B. C., and Yang, L.: An
1095 analysis of the IGBP global land-cover characterization process, *Photogrammetric
1096 engineering and remote sensing*, 65, 1021–1032, 1999.
- 1097 Lu, J., Wang, G., Chen, T., Li, S., Hagan, D. F. T., Kattel, G., Peng, J., Jiang, T., and
1098 Su, B.: A harmonized global land evaporation dataset from model-based products
1099 covering 1980–2017, *Earth System Science Data*, 13, 5879–5898,
1100 <https://doi.org/10.5194/essd-13-5879-2021>, 2021.
- 1101 Ma, N., Szilagyi, J., and Jozsa, J.: Benchmarking large-scale evapotranspiration
1102 estimates: A perspective from a calibration-free complementary relationship approach
1103 and FLUXCOM, *Journal of Hydrology*, 590,
1104 <https://doi.org/10.1016/j.jhydrol.2020.125221>, 2020.
- 1105 Majozi, N. P., Mannaerts, C. M., Ramoelo, A., Mathieu, R., Nickless, A., and Verhoef,
1106 W.: Analysing surface energy balance closure and partitioning over a semi-arid
1107 savanna FLUXNET site in Skukuza, Kruger National Park, South Africa, *Hydrology
1108 and Earth System Sciences*, 21, 3401–3415, <https://doi.org/10.5194/hess-21-3401->



- 1109 2017, 2017.
- 1110 Martens, B., Miralles, D. G., Lievens, H., van der Schalie, R., de Jeu, R. A. M.,
1111 Fernández-Prieto, D., Beck, H. E., Dorigo, W. A., and Verhoest, N. E. C.:
1112 GLEAM v3: satellite-based land evaporation and root-zone soil moisture,
1113 Geoscientific Model Development, 10, 1903–1925, [https://doi.org/10.5194/gmd-10-](https://doi.org/10.5194/gmd-10-1903-2017)
1114 1903-2017, 2017.
- 1115 McColl, K. A., Vogelzang, J., Konings, A. G., Entekhabi, D., Piles, M., and Stoffelen,
1116 A.: Extended triple collocation: Estimating errors and correlation coefficients with
1117 respect to an unknown target, *Geophysical Research Letters*, 41, 6229–6236,
1118 <https://doi.org/10.1002/2014gl061322>, 2014.
- 1119 Ming, W., Ji, X., Zhang, M., Li, Y., Liu, C., Wang, Y., and Li, J.: A Hybrid Triple
1120 Collocation-Deep Learning Approach for Improving Soil Moisture Estimation from
1121 Satellite and Model-Based Data, *Remote Sensing*, 14,
1122 <https://doi.org/10.3390/rs14071744>, 2022.
- 1123 Miralles, D., De Jeu, R., Gash, J., Holmes, T., and Dolman, A.: Magnitude and
1124 variability of land evaporation and its components at the global scale, *Hydrology and*
1125 *Earth System Sciences*, 15, 967–981, 2011.
- 1126 Miralles, D. G., Gentine, P., Seneviratne, S. I., and Teuling, A. J.: Land-atmospheric
1127 feedbacks during droughts and heatwaves: state of the science and current challenges,
1128 *Ann N Y Acad Sci*, 1436, 19–35, <https://doi.org/10.1111/nyas.13912>, 2019.
- 1129 Mu, Q., Zhao, M., and Running, S. W.: Improvements to a MODIS global terrestrial
1130 evapotranspiration algorithm, *Remote sensing of environment*, 115, 1781–1800, 2011.
- 1131 Muñoz-Sabater, J., Dutra, E., Agustí-Panareda, A., Albergel, C., Arduini, G., Balsamo,
1132 G., Boussetta, S., Choulga, M., Harrigan, S., Hersbach, H., Martens, B., Miralles, D.
1133 G., Piles, M., Rodríguez-Fernández, N. J., Zsoter, E., Buontempo, C., and Thépaut, J.-
1134 N.: ERA5-Land: a state-of-the-art global reanalysis dataset for land applications,
1135 *Earth Syst. Sci. Data*, 13, 4349–4383, <https://doi.org/10.5194/essd-13-4349-2021>,
1136 2021.
- 1137 Pan, S., Pan, N., Tian, H., Friedlingstein, P., Sitch, S., Shi, H., Arora, V. K., Haverd,
1138 V., Jain, A. K., Kato, E., Lienert, S., Lombardozzi, D., Nabel, J. E. M. S., Ottlé, C.,
1139 Poulter, B., Zaehle, S., and Running, S. W.: Evaluation of global terrestrial
1140 evapotranspiration using state-of-the-art approaches in remote sensing, machine
1141 learning and land surface modeling, *Hydrology and Earth System Sciences*, 24, 1485–
1142 1509, <https://doi.org/10.5194/hess-24-1485-2020>, 2020.
- 1143 Park, J., Baik, J., and Choi, M.: Triple collocation-based multi-source evaporation and
1144 transpiration merging, *Agricultural and Forest Meteorology*, 331, 109353, 2023.
- 1145 Pastorello, G., Trotta, C., Canfora, E., Chu, H., Christianson, D., Cheah, Y. W.,
1146 Poindexter, C., Chen, J., Elbashandy, A., Humphrey, M., Isaac, P., Polidori, D.,
1147 Reichstein, M., Ribeca, A., van Ingen, C., Vuichard, N., Zhang, L., Amiro, B.,
1148 Ammann, C., Arain, M. A., Ardo, J., Arkebauer, T., Arndt, S. K., Arriga, N., Aubinet,
1149 M., Aurela, M., Baldocchi, D., Barr, A., Beamesderfer, E., Marchesini, L. B.,
1150 Bergeron, O., Beringer, J., Bernhofer, C., Berveiller, D., Billesbach, D., Black, T. A.,



- 1151 Blanken, P. D., Bohrer, G., Boike, J., Bolstad, P. V., Bonal, D., Bonnefond, J. M.,
1152 Bowling, D. R., Bracho, R., Brodeur, J., Brummer, C., Buchmann, N., Burban, B.,
1153 Burns, S. P., Buysse, P., Cale, P., Cavagna, M., Cellier, P., Chen, S., Chini, I.,
1154 Christensen, T. R., Cleverly, J., Collalti, A., Consalvo, C., Cook, B. D., Cook, D.,
1155 Coursolle, C., Cremonese, E., Curtis, P. S., D'Andrea, E., da Rocha, H., Dai, X.,
1156 Davis, K. J., Cinti, B., Grandcourt, A., Ligne, A., De Oliveira, R. C., Delpierre, N.,
1157 Desai, A. R., Di Bella, C. M., Tommasi, P. D., Dolman, H., Domingo, F., Dong, G.,
1158 Dore, S., Duce, P., Dufrene, E., Dunn, A., Dusek, J., Eamus, D., Eichelmann, U.,
1159 ElKhidir, H. A. M., Eugster, W., Ewenz, C. M., Ewers, B., Famulari, D., Fares, S.,
1160 Feigenwinter, I., Feitz, A., Fensholt, R., Filippa, G., Fischer, M., Frank, J., Galvagno,
1161 M., et al.: The FLUXNET2015 dataset and the ONEFlux processing pipeline for eddy
1162 covariance data, *Sci Data*, 7, 225, <https://doi.org/10.1038/s41597-020-0534-3>, 2020.
- 1163 Priestley, C. H. B. and TAYLOR, R. J.: On the assessment of surface heat flux and
1164 evaporation using large-scale parameters, *Monthly weather review*, 100, 81–92, 1972.
- 1165 Restrepo-Coupe, N., Albert, L. P., Longo, M., Baker, I., Levine, N. M., Mercado, L.
1166 M., da Araujo, A. C., Christoffersen, B. O., Costa, M. H., Fitzjarrald, D. R., Galbraith,
1167 D., Imbuzeiro, H., Malhi, Y., von Randow, C., Zeng, X., Moorcroft, P., and Saleska,
1168 S. R.: Understanding water and energy fluxes in the Amazonia: Lessons from an
1169 observation-model intercomparison, *Glob Chang Biol*, 27, 1802–1819,
1170 <https://doi.org/10.1111/gcb.15555>, 2021.
- 1171 Ribal, A. and Young, I. R.: Global Calibration and Error Estimation of Altimeter,
1172 Scatterometer, and Radiometer Wind Speed Using Triple Collocation, *Remote*
1173 *Sensing*, 12, <https://doi.org/10.3390/rs12121997>, 2020.
- 1174 Rodell, M., Houser, P., Jambor, U., Gottschalck, J., Mitchell, K., Meng, C.-J.,
1175 Arsenault, K., Cosgrove, B., Radakovich, J., and Bosilovich, M.: The global land data
1176 assimilation system, *Bulletin of the American Meteorological society*, 85, 381–394,
1177 2004.
- 1178 Sheffield, J., Goteti, G., and Wood, E. F.: Development of a 50-Year High-Resolution
1179 Global Dataset of Meteorological Forcings for Land Surface Modeling, *Journal of*
1180 *Climate*, 19, 3088–3111, <https://doi.org/10.1175/JCLI3790.1>, 2006.
- 1181 Stoffelen, A.: Toward the true near-surface wind speed: Error modeling and
1182 calibration using triple collocation, *Journal of Geophysical Research: Oceans*, 103,
1183 7755–7766, <https://doi.org/10.1029/97jc03180>, 1998.
- 1184 Su, C.-H. and Ryu, D.: Multi-scale analysis of bias correction of soil moisture,
1185 *Hydrology and Earth System Sciences*, 19, 17–31, 2015.
- 1186 Su, C.-H., Ryu, D., Crow, W. T., and Western, A. W.: Beyond triple collocation:
1187 Applications to soil moisture monitoring, *Journal of Geophysical Research:*
1188 *Atmospheres*, 119, 6419–6439, <https://doi.org/10.1002/2013jd021043>, 2014.
- 1189 Sun, J., McColl, K. A., Wang, Y., Rigden, A. J., Lu, H., Yang, K., Li, Y., and
1190 Santanello, J. A.: Global evaluation of terrestrial near-surface air temperature and
1191 specific humidity retrievals from the Atmospheric Infrared Sounder (AIRS), *Remote*
1192 *Sensing of Environment*, 252, <https://doi.org/10.1016/j.rse.2020.112146>, 2021.



- 1193 Towner, J., Cloke, H. L., Zsoter, E., Flamig, Z., Hoch, J. M., Bazo, J., Coughlan de
1194 Perez, E., and Stephens, E. M.: Assessing the performance of global hydrological
1195 models for capturing peak river flows in the Amazon basin, *Hydrology and Earth
1196 System Sciences*, 23, 3057–3080, <https://doi.org/10.5194/hess-23-3057-2019>, 2019.
- 1197 Tsamalis, C.: Clarifications on the equations and the sample number in triple
1198 collocation analysis using SST observations, *Remote Sensing of Environment*, 272,
1199 <https://doi.org/10.1016/j.rse.2022.112936>, 2022.
- 1200 Twine, T. E., Kustas, W., Norman, J., Cook, D., Houser, Pr., Meyers, T., Prueger, J.,
1201 Starks, P., and Wesely, M.: Correcting eddy-covariance flux underestimates over a
1202 grassland, *Agricultural and forest meteorology*, 103, 279–300, 2000.
- 1203 Vogelzang, J., Stoffelen, A., and Verhoef, A.: The Effect of Error Non-Orthogonality
1204 on Triple Collocation Analyses, *Remote Sensing*, 14, 4268, 2022.
- 1205 Wu, K., Ryu, D., Nie, L., and Shu, H.: Time-variant error characterization of SMAP
1206 and ASCAT soil moisture using Triple Collocation Analysis, *Remote Sensing of
1207 Environment*, 256, <https://doi.org/10.1016/j.rse.2021.112324>, 2021.
- 1208 Yilmaz, M. T. and Crow, W. T.: The optimality of potential rescaling approaches in
1209 land data assimilation, *Journal of Hydrometeorology*, 14, 650–660, 2013.
- 1210 Yilmaz, M. T. and Crow, W. T.: Evaluation of Assumptions in Soil Moisture Triple
1211 Collocation Analysis, *Journal of Hydrometeorology*, 15, 1293–1302,
1212 <https://doi.org/10.1175/JHM-D-13-0158.1>, 2014.
- 1213 Yilmaz, M. T., Crow, W. T., Anderson, M. C., and Hain, C.: An objective
1214 methodology for merging satellite- and model-based soil moisture products, *Water
1215 Resources Research*, 48, n/a-n/a, <https://doi.org/10.1029/2011wr011682>, 2012.
- 1216 Yin, G. and Park, J.: The use of triple collocation approach to merge satellite- and
1217 model-based terrestrial water storage for flood potential analysis, *Journal of
1218 Hydrology*, 603, <https://doi.org/10.1016/j.jhydrol.2021.127197>, 2021.
- 1219 Yin, L., Tao, F., Chen, Y., Liu, F., and Hu, J.: Improving terrestrial evapotranspiration
1220 estimation across China during 2000–2018 with machine learning methods, *Journal of
1221 Hydrology*, 600, <https://doi.org/10.1016/j.jhydrol.2021.126538>, 2021.
- 1222 Zhang, Y., Leuning, R., Hutley, L. B., Beringer, J., McHugh, I., and Walker, J. P.:
1223 Using long-term water balances to parameterize surface conductances and calculate
1224 evaporation at 0.05 spatial resolution, *Water Resources Research*, 46, 2010.
- 1225 Zhang, Y., Kong, D., Gan, R., Chiew, F. H. S., McVicar, T. R., Zhang, Q., and Yang,
1226 Y.: Coupled estimation of 500 m and 8-day resolution global evapotranspiration and
1227 gross primary production in 2002–2017, *Remote Sensing of Environment*, 222, 165–
1228 182, <https://doi.org/10.1016/j.rse.2018.12.031>, 2019.
- 1229 Zhao, M., Liu, Y., and Konings, A. G.: Evapotranspiration frequently increases during
1230 droughts, *Nature Climate Change*, 1–7, 2022.
- 1231 Zhu, G., Li, X., Zhang, K., Ding, Z., Han, T., Ma, J., Huang, C., He, J., and Ma, T.:
1232 Multi-model ensemble prediction of terrestrial evapotranspiration across north China
1233 using Bayesian model averaging, *Hydrological Processes*, 30, 2861–2879,
1234 <https://doi.org/10.1002/hyp.10832>, 2016.



1235 Zwieback, S., Su, C.-H., Gruber, A., Dorigo, W. A., and Wagner, W.: The impact of
1236 quadratic nonlinear relations between soil moisture products on uncertainty estimates
1237 from triple collocation analysis and two quadratic extensions, *Journal of*
1238 *Hydrometeorology*, 17, 1725–1743, 2016.
1239